Electronic Structure of Polar and Semipolar $(11\bar{2}2)$-Oriented Nitride Dot-in-a-Well Systems

S. Schulz[1] and O. Marquardt[2]

[1]*Tyndall National Institute, University College Cork, Cork, Ireland*

[2]*Paul-Drude-Institut für Festkörperelektronik, Hausvogteiplatz 5-7, 10117 Berlin, Germany*

(Received 18 December 2014; revised manuscript received 30 March 2015; published 30 June 2015)

We present a detailed theoretical analysis of the electrostatic built-in fields and the electronic structures of polar and semipolar dot-in-a-well systems. Our theory is based on a symmetry-adapted multiband $\mathbf{k}\cdot\mathbf{p}$ model, parametrized by the incline angle to the wurtzite c axis, that accounts fully for the three-dimensional quantum-dot structure. As an example, we apply the model to the experimentally relevant semipolar plane $(11\bar{2}2)$. We show here that the built-in fields in isolated $(11\bar{2}2)$ semipolar quantum dots are strongly reduced compared to an equivalent c-plane structure. Our analysis further reveals that in terms of ground-state transition oscillator strength, the semipolar $(11\bar{2}2)$ dot-in-a-well systems show a superior behavior compared with their polar counterpart. We also find that increasing the InN content in the quantum dot up to a critical value leads to the unusual behavior that the ground-state electron and hole wave-function overlap increases and therefore the corresponding oscillator strength. This effect can be attributed to changes in the built-in potential profile inside the semipolar $(11\bar{2}2)$ quantum dot.

DOI: 10.1103/PhysRevApplied.3.064020

I. INTRODUCTION

For optoelectronic applications, heterostructures based on the semiconductor family AlN, InN, and GaN and their respective alloys have attracted considerable attention. In principle, their band gaps facilitate light emission from infrared to ultraviolet [1]. However, the optical properties of nitride-based heterostructures grown along the polar c axis suffer significantly from the strong electrostatic built-in fields arising from spontaneous and piezoelectric polarization [2,3]. Therefore, much research interest has been directed towards the growth of structures on semi- and nonpolar substrates [4–11]. Here, the growth direction of the heterostructure forms a nonzero angle with the polar c axis, leading to a partial or—in an ideal nonpolar quantum well (QW)—even a complete elimination of the electrostatic built-in field [4,5]. In fact, it has been demonstrated experimentally that semi- and nonpolar QWs exhibit reduced built-in fields [4,6]. However, compared to standard c-plane systems, unless grown on expensive high-quality substrates, the optical properties of semi- and nonpolar QWs are considerably affected by the existence of large densities of (extended) defects, such as basal-plane stacking faults [11–13].

An alternative to planar QW structures is the growth of semi- and nonpolar quantum dots (QDs). Their three-dimensional confinement induces a localization of carriers in a narrow spatial region and, therefore, prevents the carriers from diffusing to nearby defects, leading to nonradiative recombination. Different groups have recently focused on the growth of non- and semipolar QD structures [14–17]. Despite their potential for novel classical and also nonclassical light emitters, in comparison with QWs, little theoretical work has been directed towards *nonpolar* QDs [18–23]. Even fewer theoretical studies discuss *semipolar* QDs [18,23].

The idea of using QDs to improve the performance of optoelectronic devices could be taken even a step further by embedding these systems in a QW. This so-called dot-in-a-well (DWELL) concept has been successfully used in InGaAs-based QDs for emission in the 1200–1400 nm spectral range [24–27]. We transfer this idea to the nitride system. Here, a semipolar DWELL system should have a clear advantage over the polar system, since the semipolar plane exhibits a substantially reduced internal field and permits electrons and holes to be unhindered in diffusing across thick wells (> 4 nm). Embedded $In_{c_d}Ga_{1-c_d}N$ dots of high InN content c_d (and thus a lower band gap than the surrounding $In_{c_w}Ga_{1-c_w}N$ QW) can capture the diffusing carriers. This potentially results in efficient recombination even at longer wavelengths. A schematic illustration of this idea is given in Fig. 1. The carrier capture and the recombination processes are spatially separated, which appears to be a promising approach to achieve extremely high recombination efficiencies.

The aim of our present work is to study both polar and semipolar $In_{c_d}Ga_{1-c_d}N/In_{c_w}Ga_{1-c_w}N/GaN$ DWELLs, where c_d and c_w denote the InN content in the dot and in the well, respectively. When analyzing the electronic properties of these DWELLs, we vary both the InN content in the well (c_w) and in the dot (c_d). Due to the three-dimensional QD confinement, the theoretical description of these systems is more involved than modeling planar QW structures. Multiband $\mathbf{k}\cdot\mathbf{p}$ models are a widely used tool to compute the electronic properties of semiconductor nanostructures, such as QDs, as they combine great flexibility in the geometrical representation of nanostructures with high

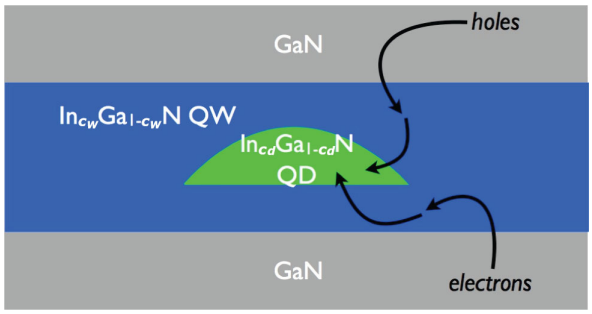

FIG. 1. Schematic illustration of an $In_{c_d}Ga_{1-c_d}N/In_{c_w}Ga_{1-c_w}N/GaN$ DWELL, where c_d and c_w denote the InN content in the dot and in the well, respectively. Assuming a semipolar substrate, the carrier transport is not being dominated by the interfacial built-in fields. The QD active region is expected to exhibit efficient carrier capture and photon emission.

computational efficiency. In combination with linear elasticity theory, to account for strain and piezoelectric potentials, these models were in the past successfully applied to answer a wide variety of questions related to semiconductor nanostructures [28–34]. To provide a continuum-based description of DWELLs grown on *semipolar* surfaces, different approaches can be selected. For instance, one approach could be to rotate the QD geometry inside the computational domain [35,36]. In this case, the standard c-plane $\mathbf{k}\cdot\mathbf{p}$ Hamiltonian, including strain and piezoelectricity, could be used. This approach could become computationally expensive since, depending on the QD geometry, the number of grid points has to be adjusted to avoid (potential) discretization problems when mapping realistic semipolar QD geometries on a grid designed for c-plane calculations. An alternative approach could be to rotate the coordinate system of the system, as discussed, for example, by Milnar *et al.* for InAs/GaAs QDs [37].

To achieve both high numerical efficiency and flexibility, we present a symmetry-adapted formalism to compute the elastic, piezoelectric, and electronic properties of semiconductor nanostructures grown along arbitrary crystallographic directions. Our formalism depends only on the angle θ between the substrate orientation and the wurtzite c axis. It should be noted that our approach is similar to the ansatz presented in Refs. [18] and [23]. However, we present complete analytic expressions for the required quantities such as stiffness tensor, polarization vector field, and (strain-dependent) $\mathbf{k}\cdot\mathbf{p}$ Hamiltonian. This approach has several benefits. For example, the derived analytic expressions allow for a more transparent analysis of the results, or for a straightforward implementation into available software packages (e.g., S/PHI/nX [38,39]); these expressions can also be directly applied to other wurtzite systems, and might be used as the starting point for analytic calculations in the framework of surface integral techniques [40,41].

As an example, we focus here on DWELLs grown on c- and $(11\bar{2}2)$-oriented substrates. The semipolar $(11\bar{2}2)$ plane has been used for growth of both (In, Ga)N QWs and QDs [6,8]. As a qualitative measure for the strength of radiative recombination, we discuss the oscillator strength of the ground-state transition, which is proportional to the corresponding spatial overlap of ground-state electron and hole wave functions. Our findings indicate that the built-in fields in *polar* DWELL systems have a detrimental effect on the oscillator strength, even in comparison to an isolated polar $In_{c_d}Ga_{1-c_d}N$ QD of the same composition. In the semipolar DWELL case, we find that the built-in field is also increased inside the dot when it is placed inside a well. However, in terms of the ground-state transition oscillator strength, the semipolar DWELL structures outperform significantly their polar counterparts. Interestingly, in the semipolar system, when keeping the InN content in the well region fixed, the oscillator strength *increases* with *increasing* QD InN content up to a critical value. Beyond this critical value, the oscillator decreases again. We show that this unexpected behavior can be attributed to changes in the complex built-in potential profile in a semipolar $(11\bar{2}2)$ DWELL. Thus, our theoretical results highlight the potential benefit of semipolar $(11\bar{2}2)$ DWELLs for future optoelectronic devices.

The paper is organized as follows. In Sec. II, we introduce the theoretical framework. Model structure and discussion of available experimental structural data on semipolar QDs are given in Sec. III. Our results are presented in Sec. IV. In Sec. IV A, we analyze the built-in potentials in polar and semipolar DWELLs in detail, while Sec. IV B focuses on their electronic structure. Our work is summarized in Sec. V.

II. THEORY

In this section, we briefly outline the theoretical framework. We refer to the appendixes for the explicit equations of the stiffness tensor and the $\mathbf{k}\cdot\mathbf{p}$ Hamiltonian. The general framework can be separated into different steps. We start with the coordinate transformation matrix for arbitrary rotations around one coordinate axis. Subsequently, we introduce the formalisms applied to compute elastic energy, spontaneous and piezoelectric polarization, and electronic properties.

A. Coordinate transformation of vectors and tensors

In order to develop a symmetry-adapted framework, we need to establish the transformation rules for vectors and tensors in general. A transformation of vectors $\mathbf{k}$ and tensors ϵ from (x, y, z) to (x', y', z') coordinates can be achieved via the expressions [42]

$$k'_i = \sum_{\alpha} U^c_{i\alpha} k_\alpha, \qquad \epsilon'_{ij} = \sum_{\alpha,\beta} U^c_{i\alpha} U^c_{j\beta} \epsilon_{\alpha\beta}. \tag{1}$$

Here, U^c denotes a unitary coordinate transformation matrix that can be written as a function of the Euler angles. For a rotation around the y axis by an angle θ, U^c reads [43]

$$U^c = \begin{pmatrix} \cos\theta & 0 & -\sin\theta \\ 0 & 1 & 0 \\ \sin\theta & 0 & \cos\theta \end{pmatrix}. \quad (2)$$

We assume that the z axis is parallel to the c axis. Making use of transformation rules given in Eq. (1), we derive stiffness tensor, strain tensor, polarization vector field, and $\mathbf{k}\cdot\mathbf{p}$ Hamiltonian as a function of the incline angle θ to the c axis.

B. Strain-field calculations

The large lattice mismatch between InN and GaN ($\sim$10%) leads to the appearance of strong strain fields in (In, Ga)N-based heterostructures. Thus, for a realistic description of the electronic and optical properties of these systems, strain effects have to be taken into account. Approaches to calculate strain fields in QD structures range from atomistic to continuum-based models [44–46]. Since the electronic-structure theory applied here is based on a continuum approach, we model the strain field in the framework of continuum elasticity [47]. Within the framework of continuum-elasticity theory, the total elastic energy F of the whole system is minimized with respect to the displacement field $\mathbf{u}$ [29]. In general, the elastic energy F of the system can be written as [48]

$$F = \frac{V}{2}\sum_{ijkl} C_{ijkl}\epsilon_{ij}\epsilon_{kl}, \quad (3)$$

where V is the volume of the system, ϵ_{ij} are the strain-tensor components, and C_{ijkl} denote the stiffness-tensor components (elastic constants). To calculate and minimize the elastic energy F for different substrate orientations, we have rotated the stiffness tensor C and calculated the elastic constants as a function of the incline angle θ. The results of this transformation are given in Appendix A. Similar approaches have been used to describe strain fields in polymorph nanowires [49] or to derive elastic constants for wurtzite from zinc-blende materials (or vice versa) [50,51].

C. Polarization vector field

Semiconductor materials without inversion symmetry exhibit an electric polarization with applied strain or stress [52]. This strain-dependent electric polarization is referred to as the piezoelectric polarization. The first-order piezoelectric-polarization vector field in a c-plane system is given by [53,54]

$$\mathbf{P}_{\text{piezo}} = \begin{pmatrix} 2e_{15}\epsilon_{xz} \\ 2e_{15}\epsilon_{yz} \\ e_{31}(\epsilon_{xx}+\epsilon_{yy}) + e_{33}\epsilon_{zz} \end{pmatrix} = \begin{pmatrix} P_{\text{shear},x} \\ P_{\text{shear},y} \\ P_{\text{axial}} \end{pmatrix}. \quad (4)$$

The strain-tensor components are denoted by ϵ_{ij}, while e_{ij} are the first-order piezoelectric coefficients. Based on the c-plane expression, Eq. (4), we denote contributions arising from the piezoelectric coefficients e_{31} and e_{33} as axial contributions, while contributions originating from e_{15} are referred to as shear-strain contributions. Making use of the transformation rules for tensors and vectors, Eq. (1), the components of the piezoelectric-polarization vector field $\mathbf{P}'_{\text{piezo}}$ in the coordinate system (x', y', z') read

$$\begin{aligned} P'_{\text{piezo},x} &= -2e_{15}\cos\theta[(\epsilon'_{xx}-\epsilon'_{zz})\cos\theta\sin\theta - \epsilon'_{xz}\cos 2\theta] \\ &\quad - e_{31}\sin\theta[\epsilon'_{yy} + \epsilon'_{xx}\cos^2\theta + \epsilon'_{xz}\sin 2\theta + \epsilon'_{zz}\sin^2\theta] \\ &\quad - e_{33}\sin\theta[\epsilon'_{zz}\cos^2\theta - \epsilon'_{xz}\sin 2\theta + \epsilon'_{xx}\sin^2\theta], \\ P'_{\text{piezo},y} &= 2e_{15}[\epsilon'_{yz}\cos\theta - \epsilon'_{xy}\sin\theta], \\ P'_{\text{piezo},z} &= -2e_{15}\sin\theta[(\epsilon'_{xx}-\epsilon'_{zz})\cos\theta\sin\theta - \epsilon'_{xz}\cos 2\theta] \\ &\quad + e_{31}\cos\theta[\epsilon'_{yy} + \epsilon'_{xx}\cos^2\theta + \epsilon'_{xz}\sin 2\theta + \epsilon'_{zz}\sin^2\theta] \\ &\quad + e_{33}\cos\theta[\epsilon'_{zz}\cos^2\theta - \epsilon'_{xz}\sin 2\theta + \epsilon'_{xx}\sin^2\theta]. \end{aligned} \quad (5)$$

Note that our result for $P'_{\text{piezo},z}$ is similar to the analytic result in Ref. [55] with one difference: the prefactor 2 in the shear-strain-related contribution in $\mathbf{P}_{\text{piezo}}$, Eq. (4), is missing in Ref. [55]. Since Romanov *et al.* [55] have focused on QWs only, no expressions for the components $P'_{\text{piezo},x}$ and $P'_{\text{piezo},y}$ are given in their work. Equation (5) shows that the expressions for these in-plane contributions are much more complicated than in the c-plane system, Eq. (4). In the c-plane structure, only shear-strain contributions occur and thus only e_{15} is involved. The component $P'_{\text{piezo},x}$ of the rotated polarization vector depends on all three piezoelectric coefficients e_{15}, e_{31}, and e_{33}.

In addition to the strain-dependent piezoelectric polarization, wurtzite nitride systems exhibit a spontaneous polarization [56]. The spontaneous-polarization vector field in the (x', y', z') coordinate system is given by

$$\begin{aligned} P'_{\text{spont},x} &= -P_{\text{SP}}\sin\theta, \\ P'_{\text{spont},y} &= 0, \\ P'_{\text{spont},z} &= P_{\text{SP}}\cos\theta. \end{aligned}$$

For $\theta = 0$, this expression reduces to the standard c-plane result [56].

The expression derived here for the spontaneous and piezoelectric polarization can now also serve as the starting point for analytic built-in field calculations in the framework of surface integral techniques. As shown, for example, by Williams *et al.* [40], for certain QD geometries, complete analytic solutions can be derived, once the full expression for the polarization vector field is known.

The corresponding built-in potential ϕ_{tot} is calculated by solving Poisson's equation,

$$\nabla[\kappa_0\kappa_r(\mathbf{r})\nabla\phi_{\text{tot}}] = -\nabla\mathbf{P}'_{\text{tot}} = \rho_{\text{tot}}, \tag{6}$$

where κ_r denotes the position-dependent dielectric constant, κ_0 the vacuum dielectric constant, and ρ_{tot} is the charge density arising from the total (spontaneous plus piezoelectric) polarization vector field $\mathbf{P}'_{\text{tot}}$.

D. Rotated k · p Hamiltonian

To calculate the valence states of wurtzite (In, Ga)N-based DWELLs grown on different substrate orientations, we use a six-band $\mathbf{k}\cdot\mathbf{p}$ formalism. We derive the $\mathbf{k}\cdot\mathbf{p}$ Hamiltonian as a function of the incline angle θ to the wurtzite c axis, giving us the flexibility to study systems grown along arbitrary crystallographic directions. Our starting point is a conventional six-band $\mathbf{k}\cdot\mathbf{p}$ Hamiltonian, designed for a (0001)-oriented system, expanded using basis states with symmetry

$$(|X\uparrow\rangle, |Y\uparrow\rangle, |Z\uparrow\rangle, |X\downarrow\rangle, |Y\downarrow\rangle, |Z\downarrow\rangle)^T.$$

The (0001)-oriented $\mathbf{k}\cdot\mathbf{p}$ Hamiltonian in this basis is taken from Ref. [57], neglecting interactions between conduction and valence bands. To obtain the six-band Hamiltonian for different substrate orientations, we proceed as described in detail by Voon *et al.* in Ref. [58]. The rotation of the $\mathbf{k}\cdot\mathbf{p}$ Hamiltonian from the [0001] direction to an arbitrary growth direction can, in general, be broken down into three steps. In the first step, one neglects the spin and rotates the basis functions of the Hamiltonian. Subsequently, the unprimed wave vector $\mathbf{k}$ and the strain tensor ϵ of the (0001)-oriented system are replaced by the primed ones, $\mathbf{k}'$ and ϵ', in the rotated system. Finally, the matrix is reexpressed in terms of the modified basis states. The rotated $\mathbf{k}\cdot\mathbf{p}$ Hamiltonian, with all matrix elements expressed as a function of the incline angle θ, and with more details of the calculation, is given in Appendix B.

To describe the electron single-particle states, we use a single-band effective mass model. Here, the Hamiltonian $\hat{H}_{\text{elec}}$ reads

$$\hat{H}_{\text{elec}} = \frac{\hbar^2}{2m_0}\frac{1}{m_e}\mathbf{k}^2 + a_c\text{Tr}(\epsilon) + V_{\text{tot}} + E_{\text{CB}}. \tag{7}$$

Since the effective electron masses parallel and perpendicular to the c axis are similar in InN and GaN [59], we assume an isotropic effective electron mass m_e. The conduction-band-edge energy is given by E_{CB}, a_c denotes the conduction-band-edge deformation potential, and $\text{Tr}(\epsilon) = \epsilon_{xx} + \epsilon_{yy} + \epsilon_{zz}$. The potential arising from spontaneous and piezoelectric polarization is denoted by V_{tot} and is related to ϕ_{tot}, Eq. (6), by $V_{\text{tot}} = -e\phi_{\text{tot}}$, with e being the elementary charge. Here, we take into account that the different quantities are position dependent.

As we discuss above, we apply our formalism to a six-band model for the valence-band structure and a one-band model for the conduction band states. The same procedure can be applied to, e.g., a full eight-band $\mathbf{k}\cdot\mathbf{p}$ model as demonstrated in Ref. [43]. Since we are mainly interested in wave-function or charge-density localization effects, transition energies are of secondary importance here. Thus, the applied formalism is already sufficient. Our theory will be extended to an eight-band model in future work.

E. Numerical implementation

The analytical expressions for stiffness tensor, strain tensor, polarization vector field, and strain-dependent $\mathbf{k}\cdot\mathbf{p}$ Hamiltonian derived as a function of the incline angle θ are implemented in the plane-wave-based software library S/PHI/nX [38,60]. Due to its generalized formulation, the equations for the different quantities can be employed without any modification of the software source code [39,61]. Only the input deck (stiffness tensor, polarization vector field, Hamiltonian) needs to be adjusted. A schematic illustration of the numerical implementation and the simulation work flow within S/PHI/nX is shown in Fig. 2.

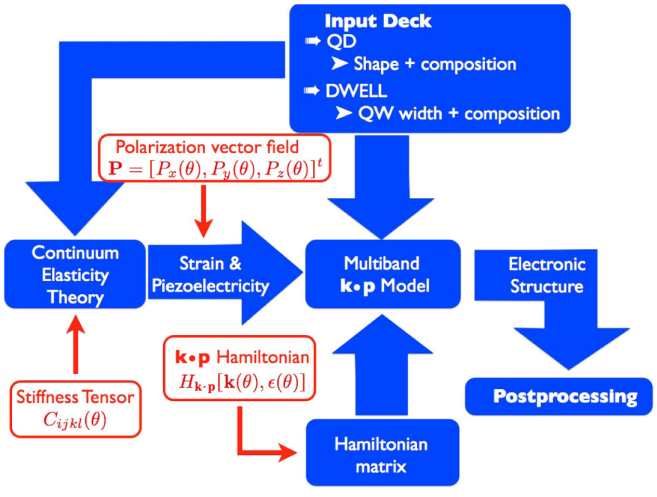

FIG. 2. Schematic illustration of the work flow in S/PHI/nX starting from the input deck parameters (compositions and geometries). The user-defined input is indicated in red.

III. DWELL-MODEL SYSTEM AND MATERIAL PARAMETERS

In this section, we introduce the model system for our calculations. A schematic illustration of the system under consideration is displayed in Fig, 1. We will use the same geometry and supercell for both polar and semipolar DWELLs. Since our main focus is on the semipolar systems, we use available experimental data on semipolar $(11\bar{2}2)$ $In_{c_d}Ga_{1-c_d}N$ QDs as input for the model geometry.

Here, we consider a lens-shaped QD in accordance with the experimental data on semipolar $(11\bar{2}2)$ QDs [15]. The QD height is 2.5 nm and the base diameter is 10 nm, similar to experimental observations [15,16]. The lens-shaped $In_{c_d}Ga_{1-c_d}N$ QD is embedded in an $In_{c_w}Ga_{1-c_w}N$ QW of 4.5-nm width. The QW InN content c_w is varied between 0% and 10%, to study the impact of the QW composition on the electronic structure of the $In_{c_d}Ga_{1-c_d}N$ QDs. The whole structure is embedded in a GaN matrix and periodic boundary conditions are applied. All calculations are carried out on supercells with dimensions of $40 \times 40 \times 40$ nm^3. Due to the cubic supercell and periodic boundary conditions, our system represents a cubic array of QDs. As discussed in detail in Refs. [53] or [62], this cubic symmetry affects the hexagonal symmetry of the underlying c-plane wurtzite lattice. However, by choosing the supercell sufficiently large, the wave functions localized inside the isolated QD are only slightly affected if they are well confined inside the QD. Furthermore, here we are interested in ground-state wave functions and InN contents larger than 25% InN in the QD. Therefore, our wave functions are localized inside or near the QD. Artifacts, introduced by the finite-size supercell, are expected to be less or equal to the uncertainty in the known values of the material parameters and their dependence on the alloy composition.

TABLE I. Material parameters for GaN and InN. Lattice constants are denoted by a_{lat} and c_{lat}, respectively. The elastic constants are given by C_{ij}, while e_{ij} are the piezoelectric coefficients. Band gaps, crystal-field splitting, and spin-orbit coupling energy are denoted by E_g, Δ_{CF}, and Δ_{SO}, respectively. The effective mass parameters are given by m_e and A_i, while the conduction- and valence-band deformation potentials are a_c and D_i, respectively. The bowing parameter for the spontaneous polarization P_{SP} is given by $b_{\mathrm{SP}}^{(\mathrm{In,Ga})\mathrm{N}}$. The band offset between InN and GaN is denoted by $\Delta E_{\mathrm{VB}}^{\mathrm{InN/GaN}}$.

Parameter	GaN	InN
a_{lat} (Å) [63]	3.180	3.542
c_{lat} (Å) [63]	5.172	5.711
C_{11} (GPa) [65]	368.6	233.8
C_{12} (GPa) [65]	131.6	110.0
C_{13} (GPa) [65]	95.7	91.6
C_{33} (GPa) [65]	406.2	238.3
C_{44} (GPa) [65]	101.7	55.4
e_{15} (C/m^2) [63]	−0.32	−0.42
e_{31} (C/m^2) [63]	−0.44	−0.58
e_{33} (C/m^2) [63]	0.74	1.07
P_{SP} (C/m^2) [63]	−0.040	−0.049
κ_r [66]	9.6	15.3
E_g (eV) [67]	3.51	0.69
Δ_{CF} (eV) [68]	0.019	0.024
Δ_{SO} (eV) [64]	0.017	0.005
m_{e} (m_0) [59]	0.209	0.068
A_1 ($\hbar^2/2m_0$) [59]	−5.947	−15.803
A_2 ($\hbar^2/2m_0$) [59]	−0.528	−0.497
A_3 ($\hbar^2/2m_0$) [59]	5.414	15.251
A_4 ($\hbar^2/2m_0$) [59]	−2.512	−7.151
A_5 ($\hbar^2/2m_0$) [59]	−2.510	−7.060
A_6 ($\hbar^2/2m_0$) [59]	−3.202	−10.078
a_c (eV) [53,64]	−4.08	−7.2
$a_c - D_1$ (eV) [68]	−5.81	−3.64
$a_c - D_2$ (eV) [68]	−8.92	−4.58
D_3 (eV) [68]	5.45	2.68
D_4 (eV) [68]	−2.97	−1.78
D_5 (eV) [68]	−2.87	−2.07
D_6 (eV) [68]	−3.95	−3.02
$b_{\mathrm{SP}}^{(\mathrm{In,Ga})\mathrm{N}}$ (C/m^2) [64]	−0.037	
$\Delta E_{\mathrm{VB}}^{\mathrm{InN/GaN}}$ (eV) [69]	0.62	

The material parameters employed are summarized in Table I. Composition-dependent bowing parameters for conduction and valence-band edge were taken from Ref. [63]. For the spontaneous polarization, we use the bowing parameter $b_{\mathrm{SP}}^{(\mathrm{In,Ga})\mathrm{N}}$ given in Ref. [64]. For all other parameters, we assume a linear interpolation.

IV. RESULTS

For a detailed discussion of our results obtained for the polar and semipolar $(11\bar{2}2)$ DWELLs, we start with the built-in potential (Sec. IV A). In Sec. IV B, we present the electronic structure of the DWELL systems and how it is modified by changing the InN content in the well and in the dot.

A. Built-in potential

Figure 3 shows the total (spontaneous plus piezoelectric) built-in potential V_{tot} in an isolated QD and in DWELLs. The InN content c_w in the well is given on top of each graph along with the In content in the dot (c_d). Figures 3(a) and 3(d) in the left column show the built-in potential V_{tot} of a polar and a semipolar $(11\bar{2}2)$ $In_{0.25}Ga_{0.75}N/GaN$ QD, respectively.

The built-in potential profile of the isolated polar $In_{0.25}Ga_{0.75}N$ QD system, Fig. 3(a), shows the well-known behavior with a strong potential drop along the c axis [53]. The close proximity of different isolines inside the QD indicates the steep slope of the potential. This steep slope leads to a strong spatial separation of electron and hole wave functions along the c axis [53]. In the corresponding semipolar case, Fig. 3(d), several interesting features are

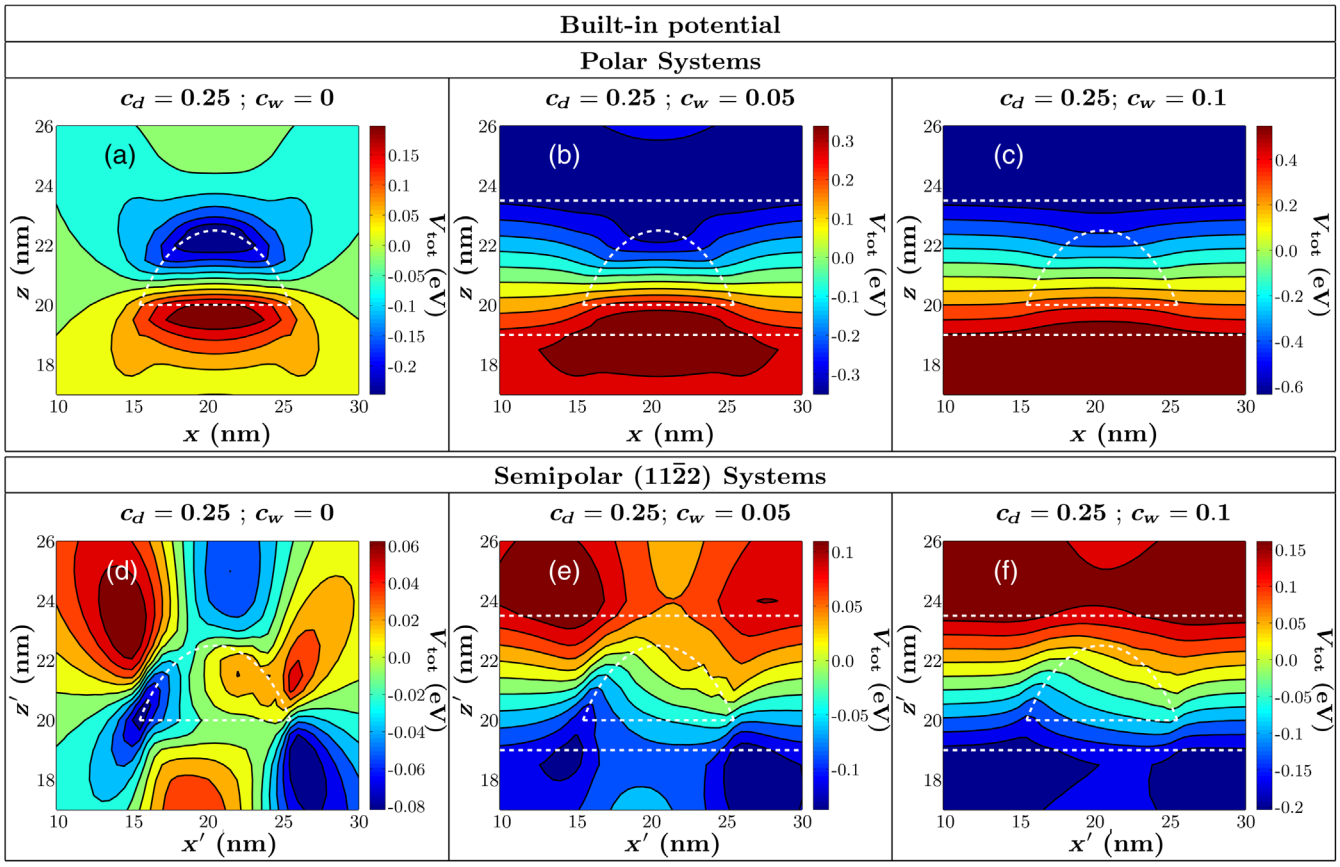

FIG. 3. Contour plots of the built-in potential in polar and semipolar (11$\bar{2}$2) DWELLs for a slice through the center of the QD. The upper part displays the results for the polar system, while the lower part depicts the results for the semipolar structures. The results are shown as a function of the InN content in the well (c_w) surrounding the $In_{0.25}Ga_{0.75}N$ QD ($c_d = 0.25$). The dashed lines indicate the QD and QW interfaces.

clearly visible. First, the built-in potential profile looks much more complicated in the semipolar case. Second, the overall potential magnitude is significantly reduced compared to the equivalent polar system [cf. Fig. 3(a)]. Third, in the semipolar case, the minima and maxima of the built-in potential are mainly outside the QD structure. Fourth, the built-in potential V_{tot} is very weak inside the semipolar QD compared with the polar system. Thus, one could expect that the spatial wave-function overlap is much higher in the semipolar QD than in the corresponding polar dot.

We turn now to the DWELL systems. The center column of Fig. 3 shows V_{tot} for the $In_{0.25}Ga_{0.75}N$ QDs embedded in a $In_{c_w}Ga_{1-c_w}N$ QW with a width of 4.5 nm and 5% InN ($c_w = 0.05$). The built-in potential is again shown for both polar and semipolar DWELLs in Figs. 3(b) and 3(e), respectively. In the right column, the InN content in the well is increased to 10% ($c_w = 0.1$). For the polar system (upper row), the magnitude of the built-in potential at the QD interfaces is increased with increasing InN content in the well. This can be explained in terms of linear continuum-elasticity theory. In this approach, the built-in potential V_{tot} of the DWELL system is the sum of the potential arising from the QW plus a contribution originating from the QD. Therefore, it can be expected that the spatial separation of electron and hole wave functions is increased with increasing InN content c_w in the well. Furthermore, when increasing c_w, not only is the built-in potential increased, but also the band-gap difference between dot and QW is reduced. Thus, the wave functions might no longer be localized in the QD region. Consequently, the DWELL concept might not be of great benefit to increase the radiative recombination rate in *polar* systems. At 10% InN in the well, Fig. 3(c), the QD structure inside the well leads only to slight changes in the otherwise parallel potential isolines.

For the semipolar (11$\bar{2}$2) DWELL structures (lower row of Fig. 3), we find a similar trend as in the polar case. Again, the magnitude of the overall built-in potential is increased with increasing QW InN content c_w. The overall magnitude of V_{tot} for an InN content of 10% in the QW, Fig. 3(f), is comparable to the magnitude of V_{tot} in an *isolated polar* QD. However, the magnitude of the built-in potential *inside* the semipolar (11$\bar{2}$2) QD is, in fact, reduced in comparison with the case of an isolated polar QD. Therefore, we expect that, as long as the electron and hole wave functions are localized inside the dot, the

spatial separation of the wave functions in the semipolar DWELL is smaller than in the equivalent polar system. We also find that the potential profile inside the semipolar DWELL is slightly changed compared with the isolated semipolar QD. In the case of the isolated QD, the wave functions will mainly be separated along the x' axis, while the potential isolines become almost parallel to the x'-y' plane in the semipolar DWELL with 10% InN in the QW [cf. Fig. 3(f)]. Thus, the spatial charge distribution could change accordingly.

For a more detailed analysis of the built-in potential profiles V_{tot}, we decompose it into contributions arising from the piezoelectric coefficients e_{33} and e_{31}, e_{15}, and the spontaneous polarization P_{SP}. As we discuss in Sec. II C, and based on the c-plane situation, we denote the contribution arising from e_{33} and e_{31} as axial. In the c-plane system, the contribution attributed to e_{15} is shear-strain related. Figure 4 shows the built-in potential originating from axial contributions (left column), the shear part (middle column), and the spontaneous polarization (right column). The upper row corresponds to the isolated *polar* $In_{0.25}Ga_{0.75}N/GaN$ QD, while the lower row shows the different contributions for the respective semipolar $(11\bar{2}2)$ system. Note that Fig. 4 shows the potential only near the QD, the full supercell is not shown.

For the polar system (upper row), the magnitude of the axial contribution, Fig. 4(a), is largest. While the axial and the spontaneous contributions, Fig. 4(c), are largest near the interfaces, the shear-strain-related part, Fig. 4(b), spreads considerably into the barrier material. For the InN content chosen here, spontaneous and shear-strain-related contributions are comparable in magnitude but opposite in sign at the upper and lower QD interface [cf. Fig. 4(b) and 4(c)]. For instance, the spontaneous contribution to the polarization potential V_{SP} is negative near the upper interface, while the shear-strain-related contribution $V_{e_{15}}$ is positive in this region. Since the magnitudes are comparable, the shear-strain-related contribution cancels parts of the spontaneous polarization contribution in and around the c-plane QD. Note that this is a direct consequence of the negative piezoelectric coefficient e_{15} [70]. Both positive and negative values for e_{15} can be found in the literature, with more recent data pointing towards a negative value [55,63,71,72]. We conclude therefore that, for the polar isolated $In_{0.25}Ga_{0.75}N/GaN$ QD, the total built-in potential V_{tot} is mainly dominated by the

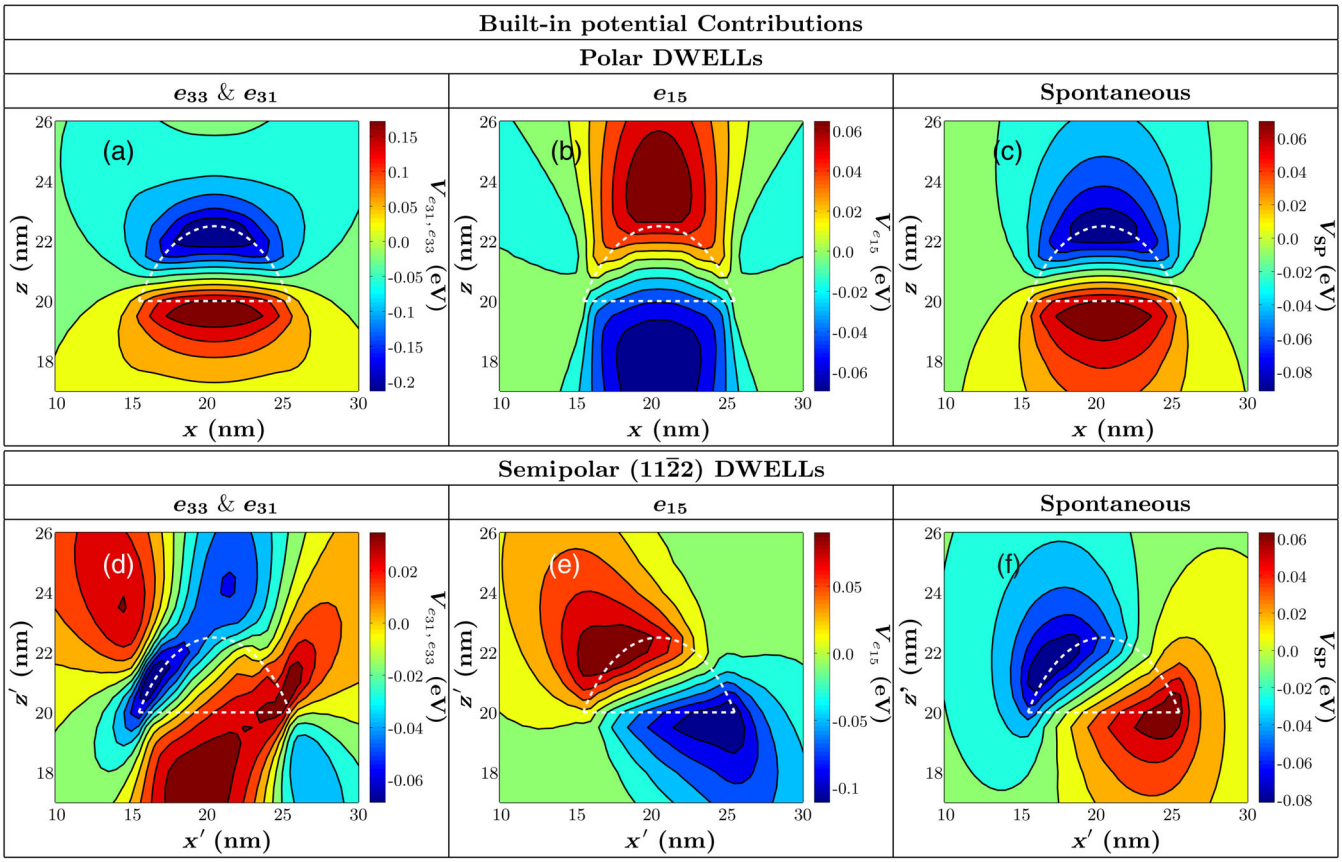

FIG. 4. Contour plots of the different contributions to the built-in potential in an isolated $In_{0.25}Ga_{0.75}N/GaN$ QD for a slice through the center of the QD. The upper part displays the results for the polar system, while the lower part depicts the results for the semipolar QD. Axial contribution: $e_{15} = 0$, $e_{33} \neq 0$, $e_{31} \neq 0$, $P_{\mathrm{SP}} = 0$; shear-strain contribution: $e_{15} \neq 0$, $e_{33} = e_{31} = 0$, $P_{\mathrm{SP}} = 0$; spontaneous contribution: $e_{15} = e_{33} = e_{31} = 0$, $P_{\mathrm{SP}} \neq 0$. The dashed lines indicate the QD interfaces.

axial contribution $V_{e_{31},e_{33}}$. This is consistent with the result shown in Fig. 3(a).

The bottom row in Fig. 4 depicts the different contributions for the isolated *semipolar* $(11\bar{2}2)$ $In_{0.25}Ga_{0.75}N/GaN$ QD. In contrast to the *c*-plane system, the contribution arising from e_{33} and e_{31} is smallest in magnitude. Similar to the *c*-plane system, the e_{15}-related contribution, Fig. 4(e), is opposite in sign to the contributions arising from e_{31}, e_{33} and spontaneous polarization. Since spontaneous and e_{15}-related contributions exhibit a similar profile, these two contributions almost cancel each other inside and outside the QD, at least for the InN content chosen here. The total built-in potential in the semipolar QD is therefore dominated by the e_{33}- and e_{31}-related contribution [cf. Fig. 4].

B. Electronic states

In the following, we analyze the electronic structures of the polar and semipolar $(11\bar{2}2)$ DWELL systems. In Sec. IV B 1, we study the role of the QW InN content c_w, while keeping the QD InN content c_d fixed at 25%. In Sec. IV B 2, we discuss the electronic structure as a function of the InN content in the QD, while keeping the InN content in the well fixed at 5% and 10%.

1. Varying InN content in the well

To analyze changes in the electronic structure when changing the substrate orientation and/or the InN content in the well, we use the oscillator strength f^{λ} of the ground-state transition as a measure. The oscillator strength f^{λ}, in general, is defined as [30]

$$f^{\lambda} = \frac{2}{m_0 \hbar \omega} |\langle \psi^{e,\lambda}_{c_d,c_w} | \mathbf{e} \cdot \mathbf{p} | \psi^{h,\lambda}_{c_d,c_w} \rangle|^2. \tag{8}$$

The index λ denotes here the polar (P) or the semipolar (SP) case. In the following, we keep the prefactor in Eq. (8) constant between different calculations, so that a relative oscillator strength (ratio of two oscillator strengths) is mainly determined by the wave-function overlap. The ground-state electron and hole wave functions are denoted by $|\psi^{e,\lambda}_{c_d,c_w}\rangle$ and $|\psi^{h,\lambda}_{c_d,c_w}\rangle$, respectively. The light polarization vector is given by $\mathbf{e}$ and $\mathbf{p}$ denotes the momentum operator. Based on the Hamiltonian in Sec. II D, the electron ground-state wave function is purely determined by *s* orbitals, i.e., $|\psi^{e,\lambda}_{c_d,c_w}\rangle \sim |S\rangle$. The hole ground-state wave function is given as a linear combination of $|X\rangle$-, $|Y\rangle$-, and $|Z\rangle$-like states: $|\psi^{h,\lambda}_{c_d,c_w}\rangle = a^X_{\uparrow}|X,\uparrow\rangle + a^X_{\downarrow}|X,\downarrow\rangle + a^Y_{\uparrow}|Y,\uparrow\rangle + a^Y_{\downarrow}|Y,\downarrow\rangle + a^Z_{\uparrow}|Z,\uparrow\rangle + a^Z_{\downarrow}|Z,\downarrow\rangle$. The expansion coefficients $a^{\alpha}_{\updownarrow}$ are obtained from the eigenvectors of the valence-band Hamiltonian given in Appendix B. For instance, we find here that the hole ground-state charge density of the isolated *c*-plane QD, due to the symmetry of the *c* plane, consists of approximately 50% $|X\rangle$- and 50% $|Y\rangle$-like states. This situation is changed in the semipolar system. Here, we find, for instance, that in the case of the isolated semipolar $(11\bar{2}2)$ QD, the hole ground state has a charge density with approximately 98% $|Y'\rangle$-like character. This originates from the fact that, in the case of the semipolar system, the strain is *anisotropic* in the growth plane, breaking the symmetry of the $|X'\rangle$- and $|Y'\rangle$-like states. Additionally, the effective masses are different along different directions, contributing to the splitting of the different states. Consequently, semipolar $(11\bar{2}2)$ QDs or DWELLs might be ideal candidates for emitters with a high degree of linear optical polarization. The detailed analysis of the optical polarization properties is beyond the scope of the present study. To evaluate Eq. (8), we need to calculate $|\langle S|p_{\alpha}|\alpha\rangle|^2$ with $\alpha \in (X, Y, Z)$. According to the results in Ref. [73] and following Refs. [30,74,75], the values of $|\langle S|p_{\alpha}|\alpha\rangle|^2$ are taken to be equal. In the following, we assume a light polarization vector of $\mathbf{e} = 1/\sqrt{2}(1,1,0)^T$.

It should be noted that in other studies (e.g., Refs. [10,19,33]), charge-density overlaps have been used to analyze the charge-carrier separation in semiconductor nanostructures. Such a scheme could give a first, qualitative insight into the spatial separation of charge carriers. However, it might fail to give quantitative results, especially for excited states, since it neglects band-mixing effects and symmetry properties of the involved wave functions. The approach presented here overcomes these limitations and provides a quantitative measure for the wave-function separation.

Figure 5 shows the *normalized* oscillator strength $\tilde{f}^{\lambda}(c_w)$ of the ground-state transition in polar (diamonds) and semipolar (squares) $In_{0.25}Ga_{0.75}N/In_{c_w}Ga_{1-c_w}N/GaN$ DWELLs as a function of the InN content c_w in the well. With the index λ denoting the polar (P) or the semipolar (SP) case, $\tilde{f}^{\lambda}(c_w)$ is defined as

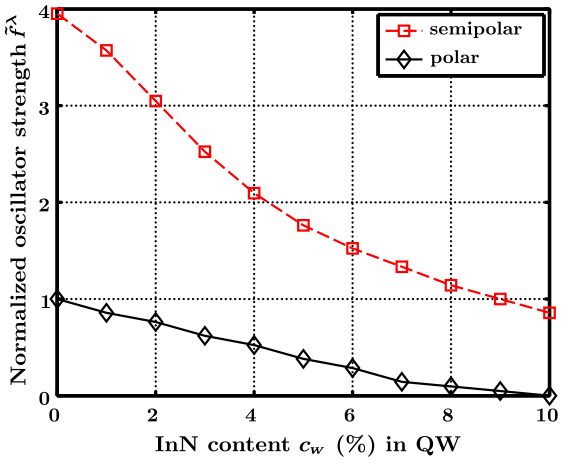

FIG. 5. Relative oscillator strength $\tilde{f}^{\lambda}$ in polar and semipolar $In_{0.25}Ga_{0.75}N/In_{c_w}Ga_{1-c_w}N/GaN$ DWELLs. The oscillator strength is shown as a function of the InN content c_w of the well. The results are normalized to the oscillator strength in the isolated ($c_w = 0$) polar $In_{0.25}Ga_{0.75}N/GaN$ QD.

$$\tilde{f}^{\lambda}(c_w) = \frac{f^{\lambda}(c_d = 0.25, c_w)}{f^{\mathrm{P}}(c_d = 0.25, c_w = 0)}. \quad (9)$$

In a first step, we analyze the normalized oscillator strength in the polar system. Due to the definition of $\tilde{f}^{\lambda}(c_w)$, Eq. (9), $\tilde{f}^{\mathrm{P}}(c_w) = 1$ if $c_w = 0$ [cf. Fig. 5]. With increasing QW InN content c_w, the normalized oscillator strength $\tilde{f}^{\mathrm{P}}(c_w)$ decreases. At 10% InN in the QW, the oscillator strength is negligible compared with the isolated polar QD [$\tilde{f}^{\mathrm{P}}(0.1) \approx 0$]. This analysis indicates that *polar* DWELL structures have inferior properties in terms of the normalized oscillator strength when compared with an isolated polar dot of the same composition.

The situation is different for the *semipolar* $(11\bar{2}2)$ DWELL systems. The normalized oscillator strength $\tilde{f}^{\mathrm{SP}}(c_w)$ is shown in (red) squares in Fig. 5. For the isolated semipolar dot ($c_w = 0$), the normalized oscillator strength of the ground-state transition is approximately four times as large as in the equivalent polar system [$\tilde{f}^{\mathrm{SP}}(0) \approx 3.9$]. This reflects the reduced built-in potential we discuss in Sec. IV A and shown in Fig. 3. With the InN content in the QW increasing, $\tilde{f}^{\mathrm{SP}}(c_w)$ decreases. However, while in the polar DWELL $\tilde{f}^{\mathrm{P}}(0.1)$ is negligible, in the semipolar case $\tilde{f}^{\mathrm{SP}}(0.1) \approx 0.9$. Even at 10% InN in the QW, the normalized oscillator strength of the ground-state transition in the semipolar DWELL is approximately equivalent to the oscillator strength in an *isolated polar* $In_{0.25}Ga_{0.75}N/GaN$ QD. This highlights that semipolar $(11\bar{2}2)$ DWELLs are promising candidates to achieve significantly improved optical recombination rates compared with polar structures.

Figure 6 displays the electron (red) and hole (green) ground-state charge densities of both polar and semipolar DWELL systems. The light and dark isosurfaces are shown at 5% and 50% of the maximum charge density, respectively. QW and QD interfaces are indicated by the dashed lines. The upper row gives the results for the *polar* $In_{0.25}Ga_{0.75}N/In_{c_w}Ga_{1-c_w}N/GaN$ DWELL system, while

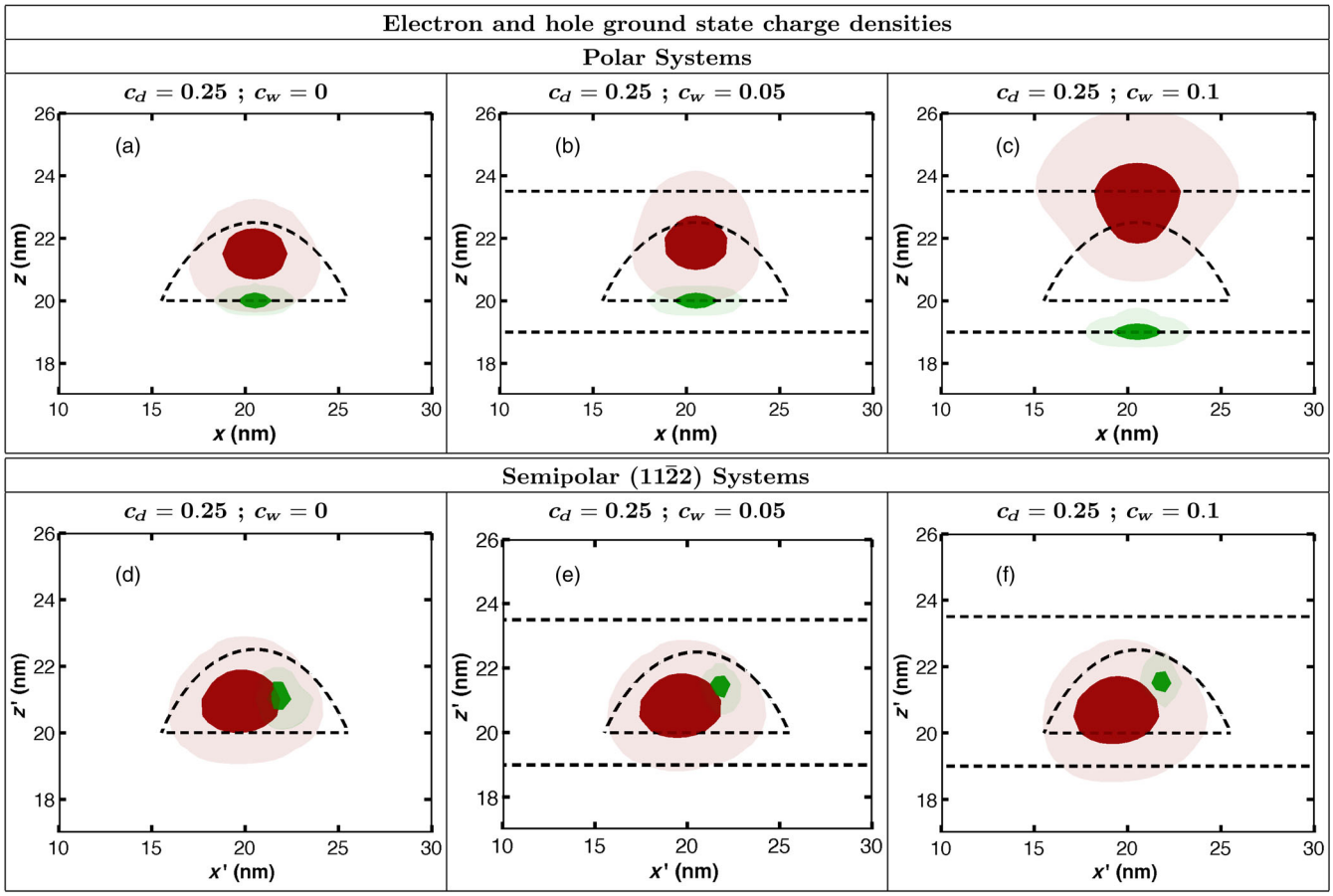

FIG. 6. Isosurfaces of the electron (red) and hole (green) ground-state charge densities in polar and semipolar DWELLs. The results are shown for a slice through the center of the QD. Light isosurfaces correspond to 5% of the maximum charge density, while the dark isosurfaces correspond to 50% of the maximum charge density. The upper part displays the data for the polar system, while the lower part depicts the charge densities for the semipolar DWELLs. Again, the InN content in the well surrounding the $In_{0.25}Ga_{0.75}N$ QD varies between $c_w = 0$ (single QD) and $c_w = 0.1$. The dashed lines indicate the QD and QW interfaces.

the lower row displays the charge densities for the *semipolar* $(11\bar{2}2)$ structures. These systems correspond to the structures considered in Fig. 5. In Fig. 6, the three columns depict the electronic structure for a QW with an InN content of $c_w = 0$, $c_w = 0.05$, and $c_w = 0.1$, respectively. In the polar system, we find that with adding more InN to the well, both electron and hole wave functions are pushed towards the interfaces of the surrounding QW. This behavior is consistent with the increase in the built-in potential that we discuss in Sec. IV A and the calculated reduction in the normalized oscillator strength $\tilde{f}^{\mathrm{P}}$ shown in Fig. 5. Figure 6 reveals that the low value of $\tilde{f}^{\mathrm{P}} \approx 0$ at $c_w = 0.1$ is caused by the localization of the hole wave function outside the QD at the lower QW interface. Likewise, the probability density of the electron wave function tends to be preferentially localized at the upper QW interface, with some contributions at the upper QD interface. With increasing well width, this effect should become more pronounced. However, it could be counterbalanced by increasing the InN content in the dot to force the wave functions back into the dot region. But in turn, the wave-function separation will also be increased inside the dot, due to the larger built-in field inside the dot. These results further support that polar DWELLs are not ideally suited for carrier-capturing processes and increased radiative transition rates.

In the semipolar systems, the situation is different, as expected from the built-in potential discussed in Sec. IV A and the results for the normalized oscillator strength $\tilde{f}^{\mathrm{SP}}(c_w)$ of the ground-state transition shown in Fig. 5. In the isolated semipolar dot [Fig. 6(d)], the built-in field is strongly reduced compared with the c-plane system, and thus the charge densities are only slightly separated along the x' axis. When increasing the InN content in the well, Figs. 6(e) and 6(f), the built-in field increases slightly and also the potential profile is slightly changed as we discuss in Sec. IV A. As shown in Figs. 6(e) and 6(f), the wave-function separation has both a component along the $(11\bar{2}2)$ growth direction (z' axis) and an in-plane component (x' axis). However, and in contrast to the polar DWELL system, the electron and hole wave functions are still localized *inside* the QD, even at 10% InN in the QW [cf. Fig. 6(f)]. Thus, the semipolar $In_{0.25}Ga_{0.75}N/In_{0.10}Ga_{0.90}N/GaN$ DWELL could be an attractive option to achieve both efficient carrier capturing and an increased radiative recombination rate due to the three-dimensional QD confinement.

2. Varying InN content in the dot

In the following section, we investigate the influence of the QD InN content c_d on the normalized oscillator strength. At first, we assume a constant QW InN content c_w of 5%. This value represents an intermediate system in terms of the relative oscillator strength [cf. Fig. 5]. We focus our attention mainly on the semipolar system. Below, we also discuss the results for the case of a QW InN content of 10% ($c_w = 0.1$).

For the semipolar $(11\bar{2}2)$ $In_{c_d}Ga_{1-c_d}N/In_{0.05}Ga_{0.95}N/GaN$ DWELL structure, we define $\tilde{f}^{\mathrm{SP}}(c_d)$, following Eq. (9), as

$$\tilde{f}^{\mathrm{SP}}(c_d) = \frac{f^{\mathrm{SP}}(c_d, c_w = 0.05)}{f^{\mathrm{P}}(c_d = 0.25, c_w = 0)}. \tag{10}$$

Even though the full InN content range is experimentally inaccessible, we vary the InN content in the dot over the full range to analyze trends in the wave-function overlap and, therefore, the relative oscillator strength. We focus our attention on first-order piezoelectricity only. Second-order effects, that might come into play at high InN contents, are neglected. Considerable work on second-order piezoelectricity has been carried out for zinc-blende materials [47,76–79]. Far less work has been dedicated to second-order piezoelectricity in wurtzite semiconductors. Therefore, the second-order piezoelectric coefficients for wurtzite InN and GaN are still far less known than their zinc-blende counterparts. For example, the wurtzite second-order coefficients derived in Ref. [72] are related to diagonal strain-tensor components ϵ_{ii} only. For c-plane QW systems, this is sufficient due to the absence of shear strain. However, Grimmer [80] has shown, based on group theory, that the second-order piezoelectric tensor for wurtzite exhibits shear-strain-related contributions. As we have seen from our analysis of first-order piezoelectricity, these shear-strain-related contributions could become very important in semipolar DWELLs. Therefore, the approach given in Ref. [72] cannot be applied to our system. Prodhomme *et al.* [81] calculated the full wurtzite second-order piezoelectric tensor using density-functional

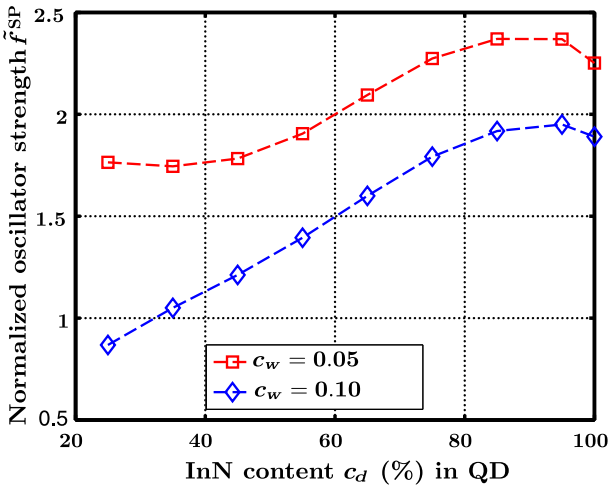

FIG. 7. Normalized ground-state transition oscillator strength $\tilde{f}^{\mathrm{SP}}$ in semipolar $In_{c_d}Ga_{1-c_d}N$ DWELLs with well InN contents $c_w = 0.05$ and $c_w = 0.10$, respectively. $\tilde{f}^{\mathrm{SP}}$ is shown as a function of the InN content c_d in the QD.

perturbation theory within local density approximation (LDA). Since LDA severely underestimates the band gap, the second-order wurtzite piezoelectric coefficients for InN are given with error bars in Ref. [81]. It is not immediately obvious how these uncertainties affect the built-in field, especially in the case of semipolar planes with different contributions canceling each other. Therefore, we include only first-order piezoelectric effects in the present study. Note that our symmetry-adapted approach to describe piezoelectricity in non-c-plane systems can easily be extended to second-order effects, once all second-order piezoelectric coefficients are known. We have previously done this in our study on (111)-oriented zinc-blende QDs [43]. With the approach presented here, no further coding is required, only the analytic expression for the second-order piezoelectric polarization field as a function of the incline angle θ has to be derived.

Figure 7 shows that the relative oscillator strength $\tilde{f}^{\mathrm{SP}}(c_d)$ for $c_w = 0.05$ stays approximately constant up to $c_d = 0.45$ and then *increases* with *increasing* InN content c_d in the dot up to $c_d = 0.85$. At a QD InN content of 85%, $\tilde{f}^{\mathrm{SP}}(0.85)$ in the semipolar $(11\bar{2}2)$ $In_{0.85}Ga_{0.15}N/In_{0.05}Ga_{0.95}N/GaN$ DWELL system is more than a factor of 2 larger than in an isolated *polar* $In_{0.25}Ga_{0.75}N/GaN$ QD. In a c-plane system, since the built-in potential increases with increasing InN content, originating from the strain dependence of the piezoelectric potential, the spatial separation between electron and hole ground-state wave functions is increased. For the semipolar $(11\bar{2}2)$ DWELL system, this decrease of the overlap is visible for $c_d > 95\%$. However, even at 100% InN in the dot, the wave-function overlap is still larger than in the semipolar system with 65% InN, as reflected in the $\tilde{f}^{\mathrm{SP}}$ values shown in Fig. 7. Compared with an isolated *polar* $In_{0.25}Ga_{0.75}N/GaN$ QD, the ground-state wave-function overlap in the semipolar $(11\bar{2}2)$ $InN/In_{0.05}Ga_{0.95}N/GaN$ DWELL is approximately a factor of 2.25 larger. Even though these very high InN contents are experimentally unrealistic, our calculations show again the potential benefit of using semipolar DWELL structures for efficient optoelectronic devices.

To understand the origin of this interesting result, Fig. 8 shows the built-in potential and the ground-state charge densities of electrons and holes in the semipolar $In_{c_d}Ga_{1-c_d}N/In_{0.05}Ga_{0.95}N/GaN$ DWELL for $c_d = 0.35$

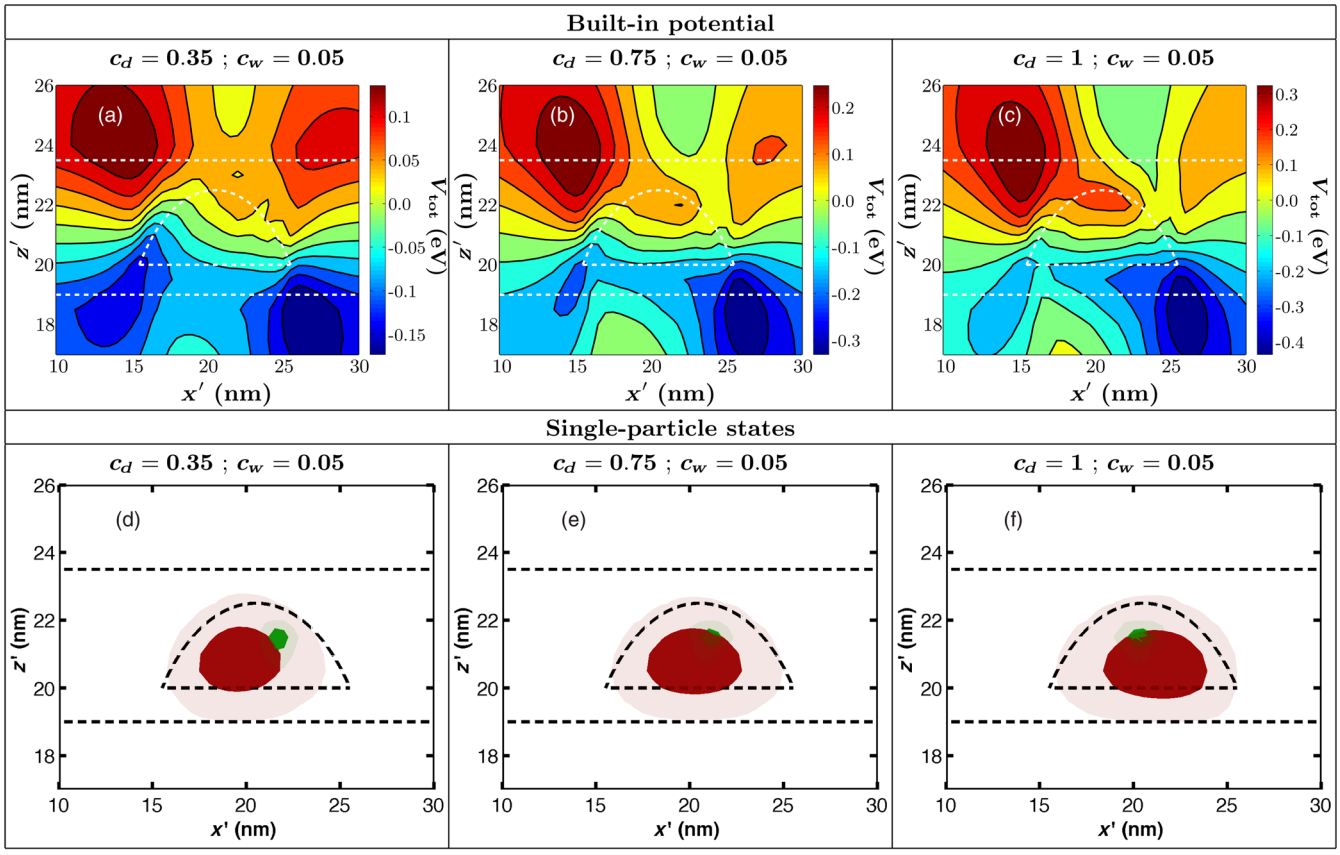

FIG. 8. Built-in potential and electron and hole ground-state charge densities in an $In_{0.35}Ga_{0.65}N/In_{0.05}Ga_{0.95}N/GaN$, an $In_{0.75}Ga_{0.25}N/In_{0.05}Ga_{0.95}N/GaN$, and an $InN/In_{0.05}Ga_{0.95}N/GaN$ DWELL, respectively. The built-in potential is shown for a slice through the center of the heterostructure. The electron (red) and hole (green) ground-state charge densities are shown at 5% and 50% of the maximum value. QD and QW interfaces are indicated by dashed lines.

(left), $c_d = 0.75$ (center), and $c_d = 1$ (right). We find that, with increasing QD InN content c_d, the magnitude of the built-in potential increases (upper row). This is expected, since increasing the InN content leads to a larger lattice mismatch and, therefore, a larger piezoelectric polarization. However, as we discuss in Sec. IV A, the extrema of the built-in potential are located mainly *outside* the QD for the semipolar system. This originates from the more complicated interplay between contributions arising from e_{15}-, e_{33}-, and e_{31}-related piezoelectric components and the spontaneous polarization [cf. Fig. 4]. Inside the QD, the built-in potential is also increased; however, in this case, the potential profile also changes. The change in the built-in potential profile leads to a change in the electron and hole wave-function localization characteristics as shown in the bottom part of Fig. 8. The charge densities show that, in the case of 35% InN ($c_d = 0.35$), the wave functions are mainly separated along the x' axis while, with increasing InN content, the wave functions are shifted towards the center of the QD. However, when comparing the results with 75% InN ($c_d = 0.75$) [cf. Fig. 8(e)] and 100% InN ($c_d = 1$) [cf. Fig. 8(f)], the electron charge density is shifted towards the bottom right corner of the QD. Additionally, at 100% InN, the electron wave function leaks further into the QW region when compared with the case for 75% InN. Thus, the electron and hole wave-function overlap should decrease slightly when comparing the $c_d = 0.75$ with the $c_d = 1$ case. This effect is consistent with the results shown in Fig. 7.

Also, the almost constant relative oscillator strength for $c_d \leq 0.45$ with $c_w = 0.05$ in Fig. 7 can be understood by looking at the charge densities. For example, when looking at the electron and hole ground-state charge densities for the $c_d = 0.35$ and $c_w = 0.05$ case [cf. Fig. 8(d)] and comparing these with the $c_d = 0.25$ and $c_w = 0.05$ situation [cf. Fig. 6(e)], there is very little difference in the charge-density localization characteristics. This is further supported by the similarities in the built-in potentials inside the QD for these two cases [Fig. 3(e) vs Fig. 8(a)]. Therefore, one could expect that the relative oscillator strength should only be slightly affected by increasing the QD InN content from 25% to 35%. This is reflected in the relative oscillator strength $\tilde{f}^{\mathrm{SP}}$ shown in Fig. 7.

In Fig. 7, we show also the result for 10% InN in the well ($c_w = 0.1$). Overall, the curve shows a similar behavior as for $c_w = 0.05$. Again, the normalized oscillator strength increases with increasing QD InN content up to 85%–95% InN. Beyond this value, the overlap decreases. However, even at $c_d = 1$ ($\mathrm{InN}/\mathrm{In_{0.1}Ga_{0.9}N}/\mathrm{GaN}$ DWELL), f^{SP} is much larger than in the isolated polar $\mathrm{In_{0.25}Ga_{0.75}N}/\mathrm{GaN}$ QD. This shows that the surprising result of an increasing wave-function overlap with increasing dot InN content is robust against changes in the QW composition. There are two main differences between the $c_w = 0.05$ and $c_w = 0.1$ cases. The first difference is that, when $c_w = 0.1$, $\tilde{f}^{\mathrm{SP}}(c_d)$ increases also in the $c_d \leq 0.45$ regime. We find in the $c_w = 0.1$ case that, when increasing c_d, the electron and hole ground-state charge densities are clearly shifted towards each other along the x' direction (not shown). This shift along the x' direction increases the spatial electron and hole ground-state wave-function overlap and, therefore, $\tilde{f}^{\mathrm{SP}}$ increases also for $c_d \leq 0.45$, as shown in Fig. 7. The second difference is that $\tilde{f}^{\mathrm{SP}}(c_d)$ is shifted to smaller values from $c_w = 0.05$ to $c_w = 0.1$. With increasing QW InN content c_w, the built-in potential of the QW is expected to start at some point to dominate the overall built-in potential profile, therefore explaining the smaller values for $\tilde{f}^{\mathrm{SP}}(c_d)$ at $c_w = 0.1$.

V. CONCLUSION

We present a detailed theoretical analysis of the built-in potential and the electronic structure of polar and semipolar $(11\bar{2}2)$ DWELL systems. Our simulations are based on a symmetry-adapted $\mathbf{k}\cdot\mathbf{p}$ approach that includes strain and polarization fields. All analytic expressions are derived as a function of the incline angle θ to the c axis and implemented in the highly flexible software package S/PHI/nX. Our model can be easily applied to QDs, DWELLs, or QWs with thickness fluctuations, grown on arbitrary wurtzite crystallographic planes that can be described by a single incline angle. As an example, we choose the semipolar plane $(11\bar{2}2)$, using available experimental data.

Isolated $(11\bar{2}2)$ semipolar QDs exhibit strongly reduced built-in fields in comparison with an equivalent polar system. As a consequence, the electron and hole ground-state wave-function overlap in the semipolar system is significantly higher than in the corresponding polar case.

Embedding an $\mathrm{In_{0.25}Ga_{0.75}N}$ c-plane QD in an $\mathrm{In}_{c_w}\mathrm{Ga}_{1-c_w}\mathrm{N}$ QW leads to a reduction of the ground-state wave-function overlap and, therefore, a reduced oscillator strength when increasing the InN content in the well. This effect arises from the increase in the built-in potential inside the QD. A similar behavior is observed in the equivalent semipolar $(11\bar{2}2)$ DWELL system. However, the effect is strongly reduced compared to the c-plane system. In the composition range that we study, the relative oscillator strength of the ground-state transition in the semipolar $(11\bar{2}2)$ DWELL is still larger than in an equivalent polar system. Thus, semipolar $(11\bar{2}2)$ DWELL systems are promising candidates for future optoelectronic devices with improved carrier capture and radiative recombination rates.

This conclusion is further supported by the finding that the relative oscillator strength increases in the semipolar $(11\bar{2}2)$ DWELLs with increasing the QD InN content, up to a critical value, for a given QW InN content. Above this critical InN value, the relative oscillator strength decreases with increasing InN content in the dot. This surprising result of an increasing wave-function overlap with increasing InN content is attributed to a change in the built-in potential profile, which results in a change of the localization of electron and

hole ground-state wave functions and, therefore, of the corresponding oscillator strength.

The results of Funato *et al.* [18] and Hong *et al.* [23] on isolated semipolar QDs indicate that the electronic structure of these systems depends on the semipolar growth plane. In future studies, our analysis of semipolar DWELLs will be extended to different growth planes and a more detailed analysis of the InN content both in the dot and in the well. Furthermore, variations of the QD size and shape will be studied to analyze their impact on the electronic and optical properties of semipolar DWELLs.

ACKNOWLEDGMENTS

S. S. acknowledges financial support from the Science Foundation Ireland (Project No. 13/SIRG/2210) and the European Union 7th Framework Programme ALIGHT (Program No. FP7-280587). We would like to thank L. Schrottke and R. Benchamekh for fruitful discussions and critical reading of the manuscript.

APPENDIX A: STIFFNESS TENSOR

Using the rotation matrix U^c defined in Eq. (2), the transformation of the stiffness tensor is

$$C'_{ijkl} = \sum_{\alpha,\beta,\gamma,\delta} U^c_{i\alpha} U^c_{j\beta} U^c_{k\gamma} U^c_{l\delta} C_{\alpha\beta\gamma\delta}, \tag{A1}$$

where $C_{\alpha\beta\gamma\delta}$ are the stiffness-tensor components of the standard c-plane system, which are given in Table I. The stiffness tensor C in the c-plane wurtzite systems in Voigt notation reads [82]

$$C = \begin{pmatrix} C_{11} & C_{12} & C_{13} & 0 & 0 & 0 \\ C_{12} & C_{11} & C_{13} & 0 & 0 & 0 \\ C_{13} & C_{13} & C_{33} & 0 & 0 & 0 \\ 0 & 0 & 0 & C_{44} & 0 & 0 \\ 0 & 0 & 0 & 0 & C_{44} & 0 \\ 0 & 0 & 0 & 0 & 0 & \frac{1}{2}(C_{11} - C_{12}) \end{pmatrix}.$$

The transformation given in Eq. (A1) yields the stiffness tensor C' for an arbitrary wurtzite growth plane characterized by the incline angle θ,

$$C' = \begin{pmatrix} C'_{11} & C'_{12} & C'_{13} & 0 & C'_{15} & 0 \\ C'_{12} & C'_{22} & C'_{23} & 0 & C'_{25} & 0 \\ C'_{13} & C'_{23} & C'_{33} & 0 & C'_{35} & 0 \\ 0 & 0 & 0 & C'_{44} & 0 & C'_{46} \\ C'_{15} & C'_{25} & C'_{35} & 0 & C'_{55} & 0 \\ 0 & 0 & 0 & C'_{46} & 0 & C'_{66} \end{pmatrix},$$

with the elastic constants

$$\begin{aligned}
C'_{11} &= \mathrm{C}_{11}\cos^4\theta + \mathrm{C}_{33}\sin^4\theta + 4\left[\frac{\mathrm{C}_{13}}{2} + \mathrm{C}_{44}\right]\cos^2\theta\sin^2\theta, \\
C'_{22} &= \mathrm{C}_{11}, \\
C'_{33} &= \mathrm{C}_{11}\sin^4\theta + \mathrm{C}_{33}\cos^4\theta + 4\left[\frac{\mathrm{C}_{13}}{2} + \mathrm{C}_{44}\right]\cos^2\theta\sin^2\theta, \\
C'_{44} &= \mathrm{C}_{44}\cos^2\theta + \frac{1}{2}[\mathrm{C}_{11} - \mathrm{C}_{12}]\sin^2\theta, \\
C'_{55} &= \mathrm{C}_{44}\left[1 - \frac{1}{2}\sin^2 2\theta\right] \\
&\quad + \cos^2\theta\sin^2\theta[\mathrm{C}_{11} - 2\mathrm{C}_{13} + \mathrm{C}_{33} - 2\mathrm{C}_{44}], \\
C'_{66} &= \frac{1}{2}[\mathrm{C}_{11} - \mathrm{C}_{12}]\cos^2\theta + \mathrm{C}_{44}\sin^2\theta, \\
C'_{12} &= \mathrm{C}_{12}\cos^2\theta + \mathrm{C}_{13}\sin^2\theta, \\
C'_{13} &= \mathrm{C}_{13}\left[1 - \frac{1}{2}\sin^2 2\theta\right] + \cos^2\theta\sin^2\theta[\mathrm{C}_{11} + \mathrm{C}_{33} - 4\mathrm{C}_{44}], \\
C'_{15} &= \cos\theta\sin\theta[\mathrm{C}_{11}\cos^2\theta - \mathrm{C}_{33}\sin^2\theta] \\
&\quad - [\mathrm{C}_{13} + 2\mathrm{C}_{44}]\cos\theta\sin\theta\cos^2 2\theta, \\
C'_{23} &= \mathrm{C}_{13}\cos^2\theta + \mathrm{C}_{12}\sin^2\theta, \\
C'_{25} &= [\mathrm{C}_{12} - \mathrm{C}_{13}]\cos\theta\sin\theta, \\
C'_{35} &= \cos\theta\sin\theta[\mathrm{C}_{11}\sin^2\theta - \mathrm{C}_{33}\cos^2\theta] \\
&\quad + [\mathrm{C}_{13} + 2\mathrm{C}_{44}]\cos\theta\sin\theta\cos^2 2\theta, \\
C'_{46} &= \cos\theta\sin\theta\left[\frac{\mathrm{C}_{11}}{2} - \frac{\mathrm{C}_{12}}{2} - \mathrm{C}_{44}\right].
\end{aligned}$$

These quantities are used as input in Eq. (3) to determine the strain field in a heterostructure grown on different crystallographic wurtzite planes.

APPENDIX B: ROTATED SIX-BAND $\mathbf{k}\cdot\mathbf{p}$ HAMILTONIAN

Following the general procedure described in Sec. II D and taking into account the transformation rules for vectors and tensors outlined in Sec. II A, the six-band Hamiltonian $H'_{\mathbf{k}\cdot\mathbf{p}}$ in the rotated frame, expanded using basis states with symmetry $(|X'\uparrow\rangle, |Y'\uparrow\rangle, |Z'\uparrow\rangle, |X'\downarrow\rangle, |Y'\downarrow\rangle, |Z'\downarrow\rangle)^T$, can be written as

$$H'_{\mathbf{k}\cdot\mathbf{p}} = \begin{pmatrix} M'(\mathbf{k}') & \Gamma'_{\mathrm{SO}} \\ -\Gamma'^{*}_{\mathrm{SO}} & M'^{*}(\mathbf{k}') \end{pmatrix}, \tag{B1}$$

where $M'(\mathbf{k}')$ and Γ'_{SO} are both 3×3 matrices. The matrix $M'(\mathbf{k}')$ can be decomposed in several submatrices,

$$M'(\mathbf{k}') = M'_{\mathrm{PE}} + M'_{\mathrm{CF}} + M'_{\mathrm{KE}} + M'_{\mathrm{str}} + M'_{\mathrm{SO}}. \tag{B2}$$

The potential energy component M'_{PE}, which contains terms independent of $\mathbf{k}'$, is given by

$$M'_{\mathrm{PE}} = \begin{pmatrix} \tilde{E}_{\mathrm{VB}} & 0 & 0 \\ 0 & \tilde{E}_{\mathrm{VB}} & 0 \\ 0 & 0 & \tilde{E}_{\mathrm{VB}} \end{pmatrix}.$$

The average unstrained valence-band edge is denoted by $\tilde{E}_{\mathrm{VB}}$, which is defined as

$$\tilde{E}_{\mathrm{VB}} = E_{\mathrm{VB}} + V_{\mathrm{tot}} - \frac{\Delta_{\mathrm{SO}}}{3}, \tag{B3}$$

where Δ_{SO} denotes the spin-orbit coupling energy. E_{VB} is the averaged valence-band edge on an absolute scale and V_{tot} is the potential arising from the total (spontaneous plus piezoelectric) built-in potential.

The crystal-field splitting component M'_{CF} is given by

$$M'_{\mathrm{CF}} = \begin{pmatrix} -\Delta_{\mathrm{CF}}\sin^2\theta & 0 & \Delta_{\mathrm{CF}}\cos\theta\sin\theta \\ 0 & 0 & 0 \\ \Delta_{\mathrm{CF}}\cos\theta\sin\theta & 0 & -\Delta_{\mathrm{CF}}\cos^2\theta \end{pmatrix},$$

with Δ_{CF} denoting the crystal-field splitting energy.

The kinetic-energy component M'_{KE} is given by

$$M'_{\mathrm{KE}} = \begin{pmatrix} h'_{11}(\mathbf{k}') & h'_{12}(\mathbf{k}') & h'_{13}(\mathbf{k}') \\ h'_{12}(\mathbf{k}') & h'_{22}(\mathbf{k}') & h'_{23}(\mathbf{k}') \\ h'_{13}(\mathbf{k}') & h'_{23}(\mathbf{k}') & h'_{33}(\mathbf{k}') \end{pmatrix},$$

with

$$\begin{aligned}
h'_{11} &= (A_2 + (A_4 + A_5)\cos^2\theta)[k'_x\cos\theta + k'_z\sin\theta]^2 + (A_1 + A_3\cos^2\theta)[k'_x\sin\theta - k'_z\cos\theta]^2 \\
&\quad + [A_2 + (A_4 - A_5)\cos^2\theta]k'^2_y + \sqrt{2}A_6[(k'^2_x - k'^2_z)\cos\theta\sin\theta - k'_xk'_z\cos 2\theta]\sin 2\theta, \\
h'_{12} &= \sqrt{2}A_6[k'_xk'_y\sin\theta - k'_yk'_z\cos\theta]\sin\theta + 2A_5[k'_xk'_y\cos\theta + k'_yk'_z\sin\theta]\cos\theta, \\
h'_{13} &= A_3\sin\theta\cos\theta[k'_x\sin\theta - k'_z\cos\theta]^2 + [A_4 + A_5]\sin\theta\cos\theta[k'_x\cos\theta + k'_z\sin\theta]^2 \\
&\quad + \sqrt{2}A_6[k'_xk'_z - (k'^2_x - k'^2_z)\cos\theta\sin\theta\cos 2\theta - 4k'_xk'_z\cos^2\theta\sin^2\theta] + (A_4 - A_5)[k'^2_y\sin\theta\cos\theta], \\
h'_{22} &= [A_1 + A_3][k'_z\cos\theta - k'_x\sin\theta]^2 + [A_2 + A_4 - A_5][k'_x\cos\theta + k'_z\sin\theta]^2 + [A_2 + A_4 + A_5]k'^2_y, \\
h'_{23} &= \sqrt{2}A_6[k'_yk'_z\cos\theta - k'_xk'_y\sin\theta]\cos\theta + 2A_5[k'_xk'_y\cos\theta + k'_yk'_z\sin\theta]\sin\theta, \\
h'_{33} &= [A_2 + (A_4 + A_5)\sin^2\theta][k'_x\cos\theta + k'_z\sin\theta]^2 + [A_1 + A_3\sin^2\theta][k'_x\sin\theta - k'_z\cos\theta]^2 \\
&\quad + [A_2 + (A_4 - A_5)\sin^2\theta]k'^2_y + \sqrt{2}A_6[k'_xk'_z\cos 2\theta + (k'^2_z - k'^2_x)\cos\theta\sin\theta]\sin 2\theta.
\end{aligned}$$

The parameters A_i play a similar role as the Luttinger parameters in a zinc-blende material.

The strain-dependent component M'_{str} can be written as

$$M'_{\mathrm{str}} = \begin{pmatrix} h'^{\mathrm{str}}_{11} & h'^{\mathrm{str}}_{12} & h'^{\mathrm{str}}_{13} \\ h'^{\mathrm{str}}_{12} & h'^{\mathrm{str}}_{22} & h'^{\mathrm{str}}_{23} \\ h'^{\mathrm{str}}_{13} & h'^{\mathrm{str}}_{23} & h'^{\mathrm{str}}_{33} \end{pmatrix}. \tag{B4}$$

The matrix elements h'^{str}_{ij} of the strain-dependent part M'_{str} of the full Hamiltonian $H'_{\mathbf{k}\cdot\mathbf{p}}$, Eq. (B1), can be obtained from the matrix elements $h'_{ij}(\mathbf{k}')$ by the simple substitution rules

$$A_i \rightarrow D_i \tag{B5}$$

$$k'_ik'_j \rightarrow \epsilon'_{ij}, \tag{B6}$$

with D_i denoting the valence-band deformation potentials.

The spin-orbit related contributions M'_{SO} and Γ'_{SO} are given by

$$M'_{\mathrm{SO}} = \frac{\Delta_{\mathrm{SO}}}{3}\begin{pmatrix} 0 & -i & 0 \\ i & 0 & 0 \\ 0 & 0 & 0 \end{pmatrix}, \quad \Gamma'_{\mathrm{SO}} = \frac{\Delta_{\mathrm{SO}}}{3}\begin{pmatrix} 0 & 0 & 1 \\ 0 & 0 & -i \\ -1 & i & 0 \end{pmatrix}. \tag{B7}$$

Possible differences of the spin-orbit coupling energy parallel ($\Delta^{\parallel}_{\mathrm{SO}}$) and perpendicular ($\Delta^{\perp}_{\mathrm{SO}}$) to the c axis are neglected. Consequently, in this quasi-cubic approximation only one spin-orbit coupling energy $\Delta_{\mathrm{SO}} = \Delta^{\perp}_{\mathrm{SO}} = \Delta^{\parallel}_{\mathrm{SO}}$ has to be considered. This is a widely used approximation [67,75,83–85], also when extracting spin-orbit coupling information from experimental data [86,87]. Due to the assumed isotropy of the spin-orbit interaction [88], the contributions M'_{SO} and Γ'_{SO} are identical to the contributions in the standard wurtzite c-plane system [57].

[1] C. J. Humphreys, Solid-state lighting, MRS Bull., **33**, 459 (2008).

[2] J. S. Im, H. Kollmer, J. Off, A. Sohmer, F. Scholz, and A. Hangleiter, Reduction of oscillator strength due to

piezoelectric fields in GaN/AlGaN quantum wells, Phys. Rev. B **57**, R9435 (1998).

[3] F. Widmann, J. Simon, B. Daudin, G. Feuillet, J. L. Rouvière, N. T. Pelekanos, and G. Fishman, Blue-light emission from GaN self-assembled quantum dots due to giant piezoelectric effect, Phys. Rev. B **58**, R15989 (1998).

[4] P. Waltereit, O. Brandt, A. Trampert, H. T. Grahn, J. Menniger, M. Ramsteiner, and K. H. Ploog, Nitride semiconductors free of electrostatic fields for efficient white light-emitting diodes, Nature (London) **406**, 865 (2000).

[5] U. T. Schwarz and M. Kneissl, Nitride emitters go nonpolar, Phys. Status Solidi RRL **1**, A44 (2007).

[6] H. Masui, S. P. DenBaars S. Nakamura, and U. K. Mishra, Nonpolar and semipolar III-nitride light-emitting diodes: Achievements and challenges, IEEE Trans. Electron Devices **57**, 88 (2010).

[7] Y. Zhao, S. Tanaka, C.-C. Pan, K. Fujito, D. Feezell, J. S. Speck, S. P. DenBaars, and S. Nakamura, High-power blue-violet semipolar (2021) InGaN/GaN light-emitting diodes with low efficiency droop at 200 A/cm^2, Appl. Phys. Express **4**, 082104 (2011).

[8] F. Scholz, Semipolar GaN grown on foreign substrates: A review, Semicond. Sci. Technol., **27**, 024002 (2012).

[9] C. C. Pan, S. Tanaka, F. Wu, Y. Zhao, J. S. Speck, S. Nakamura, S. P. DenBaars, and D. Feezell, High-power, low-efficiency-droop semipolar (2021) single-quantum-well blue light-emitting diodes, Appl. Phys. Express **5**, 062103 (2012).

[10] O. Marquardt, T. Hickel, J. Neugebauer, and C. G. van de Walle, Polarization effects due to thickness fluctuations in nonpolar InGaN/GaN quantum wells, Appl. Phys. Lett. **103**, 073115 (2013).

[11] D. Kundys, S. Schulz, F. Oehler, D. Sutherland, T. J. Badcock, P. Dawson, M. J. Kappers, R. A. Oliver, and C. J. Humphreys, Polarized photoluminescence excitation spectroscopy of *a*-plane InGaN/GaN multiple quantum wells grown on *r*-plane sapphire, J. Appl. Phys. **115**, 113106 (2014).

[12] H. Jönen, U. Rossow, H. Bremers, L. Hoffmann, M. Brendel, A. D. Dräger, S. Schwaiger, F. Scholz, J. Thalmair, J. Zweck, and A. Hangleiter, Highly efficient light emission from stacking faults intersecting nonpolar GaInN quantum wells, Appl. Phys. Lett. **99**, 011901 (2011).

[13] T. Zhu, D. Sutherland, T. J. Badcock, R. Hao, M. A. Moram, P. Dawson, M. J. Kappers, and R. A. Oliver, Defect reduction in semipolar $(11\bar{2}2)$ gallium nitride grown using epitaxial lateral overgrowth, Jpn. J. Appl. Phys. **52**, 08JB01 (2013).

[14] S. Founta, F. Rol, E. Bellet-Amalric, J. Bleuse, B. Daudin, B. Gayral, H. Mariette, and C. Moisson, Optical properties of GaN quantum dots grown on nonpolar $(11\bar{2}0)$ SiC by molecular-beam epitaxy, Appl. Phys. Lett. **86**, 171901 (2005).

[15] A. Das, G. P. Dimitrakopulos, Y. Kotsar, A. Lotsari, Th. Kehagias, Ph. Komninou, and E. Monroy, Improved luminescence and thermal stability of semipolar $(11\bar{2}2)$ InGaN quantum dots, Appl. Phys. Lett. **98**, 201911 (2011).

[16] T. Koukoula, A. Lotsari, Th. Kehagias, G. P. Dimitrakopulos, I. Häusler, A. Das, E. Monroy, Th. Karakostas, and Ph. Komninou, Structure and strain state of polar and semipolar InGaN quantum dots, Appl. Surf. Sci. **260**, 7 (2012).

[17] T. Zhu, F. Oehler, B. P. L. Reid, R. M. Emery, R. A. Taylor, M. J. Kappers, and R. A. Oliver, Nonpolar $(11\bar{2}0)$ InGaN quantum dots with short exciton lifetimes grown by metal-organic vapor phase epitaxy, Appl. Phys. Lett. **102**, 251905 (2013).

[18] M. Funato and Y. Kawakami, Excitonic properties of polar, semipolar, and nonpolar InGaN/GaN strained quantum wells with potential fluctuations, J. Appl. Phys. **103**, 093501 (2008).

[19] O. Marquardt, T. Hickel, and J. Neugebauer, Polarization-induced charge carrier separation in polar and nonpolar grown GaN quantum dots, J. Appl. Phys. **106**, 083707 (2009).

[20] K. Schuh, S. Barthel, O. Marquardt, T. Hickel, J. Neugebauer, G. Czycholl, and F. Jahnke, Strong dipole coupling in nonpolar nitride quantum dots due to Coulomb effects, Appl. Phys. Lett. **100**, 092103 (2012).

[21] S. Schulz, M. A. Caro, and E. P. O'Reilly, Prediction of strong ground state electron and hole wave function spatial overlap in nonpolar GaN/AlN quantum dots, Appl. Phys. Lett. **101**, 113107 (2012).

[22] S. Barthel, K. Schuh, O. Marquardt, T. Hickel, J. Neugebauer, F. Jahnke, and G. Czycholl, Interplay between Coulomb interaction and quantum-confined Stark-effect in polar and nonpolar wurtzite InN/GaN quantum dots, Eur. Phys. J. B **86**, 449 (2013).

[23] K. B. Hong and M. K. Kuo, Effect of piezoelectric constants in electronic structures of InGaN quantum dots, Semicond. Sci. Technol. **28**, 105006 (2013).

[24] V. M. Ustinov, N. A. Maleev, A. E. Zhukov, A. R. Kovsh, A. Yu. Egorov, A. V. Lunev, B. V. Volovik, I. L. Krestnikov, Yu. G. Musikhin, N. A. Bert, P. S. Kop'ev, Zh. I. Alferov, N. N. Ledentsov, and D. Bimberg, InAs/InGaAs quantum dot structures on GaAs substrates emitting at 1.3 μm, Appl. Phys. Lett. **74**, 2815 (1999).

[25] J. X. Chen, U. Oesterle, A. Fiore, R. P. Stanley, M. Ilegems, and T. Todaro, Matrix effects on the structural and optical properties of InAs quantum dots, Appl. Phys. Lett. **79**, 3681 (2001).

[26] H. Y. Liu, M. Hopkinson, C. N. Harrison, M. J. Steer, R. Frith, I. R. Sellers, D. J. Mowbray, and M. S. Skolnick, Optimizing the growth of 1.3 μm InAs/InGaAs dots-in-a-well structure, J. Appl. Phys. **93**, 2931 (2003).

[27] M. T. Crowley, S. C. Heck, S. B. Healy, S. Osborne, D. P. Williams, S Schulz, and E. P. O'Reilly, Long wavelength transverse magnetic polarized absorption in 1.3 μm InAs/InGaAs dots-in-a-well type active regions, Semicond. Sci. Technol. **28**, 015012 (2013).

[28] H. Jiang and J. Singh, Strain distribution and electronic spectra of InAs/GaAs self-assembled dots: An eight-band study, Phys. Rev. B **56**, 4696 (1997).

[29] O. Stier, M. Grundmann, and D. Bimberg, Electronic and optical properties of strained quantum dots modeled by 8-$\mathbf{k}\cdot\mathbf{p}$ theory, Phys. Rev. B **59**, 5688 (1999).

[30] V. A. Fonoberov and A. A. Baladin, Exctonic properties of strained wurtzite and zinc blende $GaN/Al_xGa_{1-x}N$, J. Appl. Phys. **94**, 7178 (2003).

[31] S. L. Chuang and C. S. Chang, $\mathbf{k}\cdot\mathbf{p}$ method for strained wurtzite semiconductors, Phys. Rev. B **54**, 2491 (1996).

[32] R. Seguin, A. Schliwa, S. Rodt, K. Potschke, U. W. Pohl, and D. Bimberg, Size-Dependent Fine-Structure Splitting in Self-Organized InAs/GaAs Quantum Dots, Phys. Rev. Lett. **95**, 257402 (2005).

[33] O. Marquardt, C. Hauswald, M. Wölz, L. Geelhaar, and O. Brandt, Luminous efficiency of axial $In_xGa_{1-x}N/GaN$ nanowire heterostructures: Interplay of polarization and surface potentials, Nano Lett. **13**, 3298 (2013).

[34] *Multi-Band Effective Mass Approximations: Advanced Mathematical Models and Numerical Techniques*, Lecture Notes in Computional Science and Engineering, Vol. 94, edited by M. Ehrhardt and T. Koprucki (Springer, London, 2014).

[35] C. Cornet, A. Schliwa, J. Even, F. Dore, C. Celebi, A. Letoublon, E. Mace, C. Paranthoen, A. Simon, P. M. Koenraad, N. Bertru, D. Bimberg, and S. Loualiche, Electronic and optical properties of InAs/InP quantum dots on InP(100) and InP(311)B substrates: Theory and experiment, Phys. Rev. B **74**, 035312 (2006).

[36] A. Schliwa, M. Winkelnkemper, A. Lochmann, E. Stock, and D. Bimberg, In(Ga)As/GaAs quantum dots grown on a (111) surface as ideal sources of entangled photon pairs, Phys. Rev. B **80**, 161307 (2009).

[37] V. Mlinar and F. M. Peeters, Influence of the substrate orientation on the electronic and optical properties of InAs/GaAs quantum dots, Appl. Phys. Lett. **89**, 261910 (2006).

[38] O. Marquardt, S. Boeck, C. Freysoldt, T. Hickel, and J. Neugebauer, Plane-wave implementation of the real-space $\mathbf{k}\cdot\mathbf{p}$ formalism and continuum elasticity theory, Comput. Phys. Commun. **181**, 765 (2010).

[39] O. Marquardt, S. Boeck, C. Freysoldt, T. Hickel, S. Schulz, J. Neugebauer, and E. P. O'Reilly, A generalized plane-wave formulation of $\mathbf{k}\cdot\mathbf{p}$ formalism and continuum-elasticity approach to elastic and electronic properties of semiconductor nanostructures, Comput. Mater. Sci. **95**, 280 (2014).

[40] D. P. Williams, A. D. Andreev, E. P. O'Reilly, and D. A. Faux, Derivation of built-in polarization potentials in nitride-based semiconductor quantum dots, Phys. Rev. B **72**, 235318 (2005).

[41] D. P. Williams, S. Schulz, A. D. Andreev, and E. P. O'Reilly, Theory of GaN quantum dots for optical applications, IEEE J. Sel. Top. Quantum Electron., **15**, 1092 (2009).

[42] J. M. Hinckley and J. Singh, Influence of substrate composition and crystallographic orientation on the band structure of pseudomorphic Si-Ge alloy films, Phys. Rev. B **42**, 3546 (1990).

[43] S. Schulz, M. A. Caro, E. P. O'Reilly, and O. Marquardt, Symmetry-adapted calculations of strain and polarization fields in (111)-oriented zinc blende quantum dots, Phys. Rev. B **84**, 125312 (2011).

[44] C. Pryor, J. Kim, L. W. Wang, A. J. Williamson, and A. Zunger, Comparison of two methods for describing the strain profiles in quantum dots, J. Appl. Phys. **83**, 2548 (1998).

[45] D. Barettin, S. Madsen, B. Lassen, and M. Willatzen, Computational methods for electromechanical fields in self-assembled quantum dots, Commun. Comput. Phys. **11**, 797 (2012).

[46] D. Barettin, S. Madsen, B. Lassen, and M. Willatzen, Comparison of wurtzite atomistic and piezoelectric continuum strain models: Implications for the electronic band structure, Superlattices Microstruct. **47**, 134 (2010).

[47] A. Schliwa, M. Winkelnkemper, and D. Bimberg, Impact of size, shape, and composition on piezoelectric effects and electronic properties of In(Ga)As/GaAs quantum dots, Phys. Rev. B **76**, 205324 (2007).

[48] C. Kittel, *Introduction to Solid State Physics* (John Wiley & Sons, New York, 1995).

[49] D. Barettin, A. V. Platonov, A. Pecchia, V. N. Kats, G. E. Cirlin, I. P. Soshnikov, A. D. Bouravleuv, L. Besombes, H. Mariette, M. Auf der Maur, and A. D. Carlo, Model of a GaAs quantum dot embedded in a polymorph AlGaAs nanowire, IEEE J. Sel. Top. Quantum Electron. **19**, 1901209 (2013).

[50] R. W. Martin, Relation between elastic tensors of wurtzite and zinc-blende structure materials, Phys. Rev. B **6**, 4546 (1972).

[51] A. F. Wright, Elastic properties of zinc-blende and wurtzite AlN, GaN, and InN, J. Appl. Phys. **82**, 2833 (1997).

[52] W. G. Cady, *Piezoelectricity* (McGraw-Hill, New York, 1946).

[53] A. D. Andreev and E. P. O'Reilly, Theory of the electronic structure of GaN/AlN hexagonal quantum dots, Phys. Rev. B **62**, 15851 (2000).

[54] S. Schulz, A. Berube, and E. P. O'Reilly, Polarization fields in nitride-based quantum dots grown on nonpolar substrates, Phys. Rev. B **79**, 081401(R) (2009).

[55] A. E. Romanov, T. J. Baker, S. Nakamura, and J. S. Speck, Strain-induced polarization in wurtzite III-nitride semipolar layers, J. Appl. Phys. **100**, 023522 (2006).

[56] F. Bernardini, V. Fiorentini, and D. Vanderbilt, Spontaneous polarization and piezoelectric constants of III-V nitrides, Phys. Rev. B **56**, R10024 (1997).

[57] S. Schulz, T. J. Badcock, M. A. Moram, P. Dawson, M. J. Kappers, C. J. Humphreys, and E. P. O'Reilly, Electronic and optical properties of nonpolar *a*-plane GaN quantum wells, Phys. Rev. B **82**, 125318 (2010).

[58] L. C. Lew Yan Voon and M. Willatzen, *The* $\mathbf{k}\cdot\mathbf{p}$ *Method: Electronic Properties of Semiconductors* (Springer, Heidelberg, 2009).

[59] P. Rinke, M. Winkelnkemper, A. Qteish, D. Bimberg, J. Neugebauer, and M. Scheffler, Consistent set of band parameters for the group-III nitrides AlN, GaN, and InN, Phys. Rev. B **77**, 075202 (2008).

[60] S. Boeck, C. Freysoldt, A. Dick, L. Ismer, and J. Neugebauer, The object-oriented DFT program library S/PHI/nX, Comput. Phys. Commun. **182**, 543 (2011).

[61] O. Marquardt, S. Schulz, C. Freysoldt, S. Boeck, T. Hickel, E. P. O'Reilly, and J. Neugebauer, A flexible, plane-wave based multiband model, Opt. Quantum Electron. **44**, 183 (2012).

[62] N. Baer, S. Schulz, P. Gartner, S. Schumacher, G. Czycholl, and F. Jahnke, Influence of symmetry and Coulomb-correlation effects on the optical properties of nitride quantum dots, Phys. Rev. B **76**, 075310 (2007).

[63] M. A. Caro, S. Schulz, and E. P. O'Reilly, Theory of local electric polarization and its relation to internal strain: Impact on the polarization potential and electronic properties of group-III nitrides, Phys. Rev. B **88**, 214103 (2013).
[64] I. Vurgaftman and J. R. Meyer, Band parameters for nitrogen-containing semiconductors, J. Appl. Phys. **94**, 3675 (2003).
[65] M. A. Caro, S. Schulz, and E. P. O'Reilly, Hybrid functional study of the elastic and structural properties of wurtzite and zinc-blende group-III nitrides, Phys. Rev. B **86**, 014117 (2012).
[66] M. A. Caro, S. Schulz, S. B. Healy, and E. P. O'Reilly, Built-in field control in alloyed *c*-plane III-N quantum dots and wells, J. Appl. Phys. **109**, 084110 (2011).
[67] J. Wu, When group-III nitrides go infrared: New properties and perspectives, J. Appl. Phys. **106**, 011101 (2009).
[68] Q. Yan, P. Rinke, M. Winkelnkemper, A. Qteish, D. Bimberg, M. Scheffler, and C. G. Van de Walle, Band parameters and strain effects in ZnO and group-III nitrides, Semicond. Sci. Technol. **26**, 014037 (2011).
[69] P. G. Moses, M. Miao, Q. Yan, and C. G. Van de Walle, Hybrid functional investigations of band gaps and band alignments for AlN, GaN, InN, and InGaN, J. Chem. Phys. **134**, 084703 (2011).
[70] S. Schulz and E. P. O'Reilly, Built-in fields in stacked InGaN/GaN quantum dots, Phys. Status Solidi A **208**, 1551 (2011).
[71] K. Shimada, First-principle determination of piezoelectric stress and strain constants of wurtzite III-V nitrides, Jpn. J. Appl. Phys. **45**, L358 (2006).
[72] J. Pal, G. Tse, V. Haxha, M. A. Migliorato, and S. Tomic, Second-order piezoelectricity in wurtzite III-N semiconductors, Phys. Rev. B **84**, 085211 (2011).
[73] M. Suzuki and T. Uenoyama, Theoretical study of momentum matrix elements of GaN, Jpn. J. Appl. Phys. **35**, 543 (1996).
[74] J. Bhattacharyya, S. Ghosh, and H. T. Grahn, Are AlN and GaN substrates useful for the growth of nonpolar nitride films for UV emission? The oscillator strength perspective, Phys. Status Solidi B **246**, 1184 (2009).
[75] A. Arora and S. Ghosh, Polarization of emission from nonpolar III-nitride quantum wells: The influence of confinement, J. Phys. D **47**, 045101 (2014).
[76] G. Bester, X. Wu, D. Vanderbilt, and A. Zunger, Importance of Second-Order Piezoelectric Effects in Zinc Blende Semiconductors, Phys. Rev. Lett. **96**, 187602 (2006).
[77] G. Bester, A. Zunger, X. Wu, and D. Vanderbilt, Effects of linear and nonlinear piezoelectricity on the electronic properties of InAs/GaAs quantum dots, Phys. Rev. B **74**, 081305(R) (2006).
[78] A. Beya-Wakata, P.-Y. Prodhomme, and G. Bester, First- and second-order piezoelectricity in III-V semiconductors, Phys. Rev. B **84**, 195207 (2011).
[79] M. A. Caro, S. Schulz, and E. P. O'Reilly, Origin of nonlinear piezoelectricity in III-V semiconductors: Internal strain and bond ionicity from hybrid-functional density functional theory, Phys. Rev. B **91**, 075203 (2015).
[80] H. Grimmer, The piezoelectric effect of second order in stress or strain: Its form for crystals and quasicrystals of any symmetry, Acta Crystallogr. Sect. A **63**, 441 (2007).
[81] P.-Y. Prodhomme, A. Beya-Wakata, and G. Bester, Nonlinear piezoelectricity in wurtzite semiconductors, Phys. Rev. B **88**, 121304(R) (2013).
[82] J. F. Nye, Physical Properties of Crystals: Their Representation by Tensors and Matrices (Oxford University Press, New York, 1985).
[83] E. Sakalauskas, H. Behmenburg, C. Hums, P. Schley, G. Rossbach, C. Giesen, M. Heuken, H. Kalisch, R. H. Jansen, J. Bläsing, A. Dadgar, A Krost, and R. Goldhahn, Dielectric function and optical properties of Al-rich AlInN alloys pseudomorphically grown on GaN, J. Phys. D **43**, 365102 (2010).
[84] H.-H. Huang and Y.-R. Wu, Study of polarization properties of light emitted from *a*-plane InGaN/GaN quantum well-based light emitting diodes, J. Appl. Phys. **106**, 023106 (2009).
[85] S. Schade, U. T. Schwarz, T. Wernike, M. Weyers, and M. Kneissl, Impact of band structure and transition matrix elements on polarization properties of the photoluminescence of semipolar and nonpolar InGaN quantum wells, Phys. Status Solidi B **248**, 638 (2011).
[86] P. D. C. King, T. D. Veal, P. H. Jefferson, C. F. McConville, T. Wang, P. J. Parbrook, H. Lu, and W. J. Schaff, Valence band offset of InN/AlN heterojunctions measured by x-ray photoelectron spectroscopy, Appl. Phys. Lett. **90**, 132105 (2007).
[87] G. Rossbach, M. Feneberg, M. Röppischer, C. Werner, N. Esser, C. Cobet, T. Meisch, K. Thonke, A. Dadgar, J. Bläsing, A. Krost, and R. Goldhahn, Influence of exciton-phonon coupling and strain on the anisotropic optical response of wurtzite AlN around the band edge, Phys. Rev. B **83**, 195202 (2011).
[88] It should be noted that, in principle, the spatial transformation given by U^c has to be combined with a transformation in spin space. However, it can be shown that the spin-orbit-coupling matrix elements are independent of the chosen orientation of the basis states with symmetry $(|X\rangle, |Y\rangle, |Z\rangle)^T$, if the spin-orbit interaction is isotropic.